Modelling the Thermal Structure and Circulations of Lake Nam Co, Central Tibetan Plateau

Yang Wu[1,2], Anning Huang[1,*], Youyu Lu[3], Lazhu[4], Bo Qiu[1], Zhiqi Zhang[1], Xindan Zhang[1,2]

1. CMA-NJU Joint Laboratory for Climate Prediction Studies, School of Atmospheric Sciences, Nanjing University, Nanjing, 210023, China
2. State Key Laboratory of Severe Weather and Joint Center for Atmospheric Radar Research of CMA/NJU, School of Atmospheric Sciences, Nanjing University, Nanjing, 210023, China
3. Fisheries and Oceans Canada, Bedford Institute of Oceanography, Dartmouth, Nova Scotia, B2Y 4A2, Canada; Email: Youyu.Lu@dfo-mpo.gc.ca
4. Key Laboratory of Tibetan Environment Changes and Land Surface Processes, Institute of Tibetan Plateau Research, Chinese Academy of Sciences, Beijing, 100101,China

Corresponding author:

Prof. Anning Huang, CMA-NJU Joint Laboratory for Climate Prediction Studies, School of Atmospheric Sciences, Nanjing University, No.163 Xianlin Avenue, Nanjing, Jiangsu, China, 210023. E-mail: anhuang@nju.edu.cn;

Abstract

A three-dimensional (3-D) hydrodynamic model based on Princeton Ocean Model (POM) and a one-dimensional (1-D) lake model are applied to simulate the thermal structure and circulations of Lake Nam Co (LNC), the second largest lake in Tibet. Results show that POM can well reproduce the seasonal and synoptic variations of the in-situ observed vertical temperature profile, and the spatial distribution of satellite estimated lake surface temperature during May-December 2013. However, without considering the water and energy exchanges related to the lake hydrodynamics, the 1-D model exhibits much more evident biases in the lake thermal evolution. These shortages of the 1-D lake model solutions emphasize that the complex temperature-current interactions must be accounted for investigating the thermodynamics in large lakes over Tibet. From both observation and hydrodynamic simulations, LNC is identified to experience the springtime overturning, warm stratified phase during early-June to mid-November, autumnal overturning, and weak inverse stratified phase since mid-December. The two overturning processes last for about one month and are both related to the thermal bar development, which is controlled by the density-driven convection associated with the radiative heating (surface cooling) in spring (autumn). During the warm stratified phase, the eastern shallow basin is mainly characterized by anticyclonic circulation and bowl-shaped thermocline, while the central deep basin is featured by a cyclonic gyre (eastward

currents) and dome-shaped (bowl-shaped) thermocline with the enhancement (weakness) of thermal stratification. The lake circulation during December is basically dominated by a single strong cyclonic gyre in the main lake basin.

1. Introduction

Lake-air interactions have been an important research hotspot in understanding the multiscale water and energy balances of the complex hydroclimatic systems (Sharma et al., 2018), especially over the lake-rich regions such as Tibetan Plateau (TP), which harbors the highest alpine lake concentrations among the world (Zhang, 2018). The total number and surface areas of the lake clusters distributed across TP exceed 1500 and 47000 km^2, respectively (Ma et al., 2011; Song et al., 2014). Such a huge amount of endorheic lakes exerts significant interactive impacts on the regional weather and climate by directly influencing the turbulent fluxes and the atmospheric boundary structure (Biermann et al., 2014; Zhu et al., 2017). Additionally, most TP lakes are continuously undergoing the rapid expansion processes (Guo et al., 2019; Zhang et al., 2017), which is closely associated with the glaciers retreat, permafrost degradation, and evaporation/rainfall variations under the background of the pronounced climate warming over TP (Wang et al., 2017b). All of these concerns have brought renewed attention to explore the thermal evolution regimes and hydrological cycling features of these TP lakes and their roles in the coupled lake-atmosphere ecosystem (Huang et al., 2017; Lei et al., 2014; Su et al., 2019; Wu et al., 2019; Yang et al., 2018).

During recent years, more field measurements and satellite observations are employed with various applications for exploring the complexities of TP lakes'

74 thermal features and understanding their impacts on the overlying atmosphere.
75 (Gerken et al., 2013a; Li et al., 2018; Liu et al., 2015; Qi et al., 2019; Wang et al.,
76 2015, 2017a; Wan et al., 2014). Based on the 2-yr in-situ water temperature records,
77 Wang et al. (2019) demonstrated that LNC, the second largest lake in central TP, is a
78 typical dimictic lake with different evolution of thermal stratification within its main
79 and eastern small basins. The different stratified structures are speculated to be
80 attributed to the distinctive spatial variability of heat capacity, which is modulated by
81 the lake morphometry (i.e. basin size, lake depth, and water volume) and water
82 transparency. Analogous summer thermocline developments are also observed in
83 many other high-altitude dimictic or meromictic TP lakes, i.e. Lake Bangong Co,
84 Lake Puma YumCo, Lake Dagze Co, and Lake Tangra YumCo (Murakami et al., 2007;
85 Wang et al., 2010; Wang et al., 2014). Due to the active lake-air interaction at
86 multi-timescales, the TP lakes are documented as the important moisture sources for
87 the low-level atmosphere and play critical roles in modulating the turbulent heat
88 fluxes and therefore the atmospheric boundary stability. For example, the evaporation
89 of LNC accounts for approximate 30% of the local atmospheric water vapor and
90 favors for the abundant convection during summer monsoon periods (Xu et al., 2011;
91 Haginoya et al., 2009), which is also the analogous situation for Lake Qinghai and
92 Erhai Lake (Cui and Li 2014; Haginoya et al., 2012). Throughout the ice-free period
93 of Lake Ngoring, the biggest freshwater lake in the Yellow River source region, the

positive lake-air temperature differences lead to the vast upward sensible/latent heat fluxes and favors to maintain the persistent unstable atmospheric boundary layer (Li et al., 2015).

To make up the temporal discontinuity and spatial scarcity of observational data, numerical models have been recently adopted as effective tools for systematically assessing and gaining more insights into the interactions between TP lake thermodynamics and the atmospheric conditions (Ao et al., 2018; Dai et al., 2018a; Lazhu et al., 2016; Zhang et al., 2016). By adopting the air-lake coupled Weather Research and Forecasting Model (WRF), Wu et al. (2019) reveals that due to the warming (cooling) lag effects induced by the large water thermal inertia, most lakes in the southeastern central TP exhibit significant daytime cooling (nighttime warming) effects on the overlying atmosphere, and thus dampen the diurnal variations of 2-m air temperature. During daytime (nighttime), the lake-land thermal contrast related to the colder (warmer) water surfaces over LNC tends to generate over-lake divergent (convergent) airflow, which would further interact with the valley (mountain) breeze to suppress (stimulate) the convective activities over and downstream the lake (Gerken et al., 2013b; Yang et al., 2015). At the seasonal time scale, the Ngoring and Gayring Lake are found to decrease the air temperature variability and promote more nighttime convective rainfall during July to October (Wen et al., 2015). Xu et al.

(2019) demonstrated that Erhai lake has predominant impacts on decreasing (increasing) air temperature and atmospheric boundary layer height during daytime (nighttime), and the local circulations therein can be fully developed throughout the pre-monsoon period.

To date, the aforementioned offline or coupled representations of the TP lake thermodynamics are all accomplished by one-dimensional (1-D) lake models, i.e. the Freshwater Model based on self-similarity theory (Mironov 2008) or the Hostetler model with parameterized wind-driven eddy thermal diffusion (Hostetler et al., 1993; Subin et al., 2012). The above 1-D lake models are all designed with different physical concepts and varying levels of simplification in lake processes. During recent years, considerable calibrations of keyparameters including water/ice albedo, light attenuation coefficient, surface roughness length, and vertical mixing parameterization have been proceeded to refine the 1-D lake models' performance in depicting the diurnal/seasonal characteristics of turbulent lake-air heat exchanges and the lake thermodynamics (Dai et al., 2018b; Huang et al., 2019; Kirillin et al., 2017; Wen et al. 2016; Xu et al., 2015). However, there still exist large disadvantages for the 1-D lake models to realistically capture the thermal bar formation, springtime lake warming processes, summer dome/bowl-shaped thermocline, and destratification/overturning characteristics in autumn-winter for large thermally

stratified lakes (Bennington et al., 2014; Martynov et al., 2010; Notaro et al., 2013; Xiao et al., 2016). These unsatisfactory model discrepancies imply that in addition to the local-scale lake-air feedback or oversimplified vertical thermodynamics resolved by the 1-D lake models, a comprehensive representation of three dimensional (3-D) temperature-current interactions must be accounted for better simulating the energy redistribution within lakes and thus the evolution features of the limnological phenomena mentioned above. Specifically, a nearshore-offshore temperature gradient that is commonly stimulated by the differential heating rate between the shallower coastal and deeper mid-lake regions (Monismith et al., 1990) could last for several months in large deep lake systems (Blokhina and Selin, 2019). Such persistent thermal gradients can not only directly affect the advective heat transport across the thermal front, but also work in concert with the Coriolis force and wind stress to determine the water currents, both of which lead to the lake mixing processes much more complicated (Beletsky et al., 2012; Huang et al., 2010; Rao and Schwab 2007; Xue et al., 2015). Besides, the wind-wave-induced Langmuir circulation and the Ekman pumping transport associated with the wind stress vorticity can also jointly modify the 3-D lake circulation and heat transport (Aijaz et al., 2017; Bennington et al., 2010; Gill 1982). These complex mixing processes related to the basin-scale or local-scale gyres/currents driven by the baroclinic stratification and wind stress curl are missing in 1-D lake models, where the mixing adjustment is simplified as vertical

and determined by the wind speed and convective instability (Gu et al., 2015). The inadequate physical representations would ultimately worsen the model performances in simulating the spatiotemporal variations of large-lake thermodynamics (Leon et al., 2007; Long et al., 2007; Xue et al., 2016). The comparisons between the 1-D lake-air coupled model simulations and 3-D lake-air coupled model simulations on the Lake Victoria further confirm that precluding the flow-dependent heat transport from the heat surplus regions to cold regions directly leads to the degraded simulation in both the surface water temperature pattern and the lake-effected wind/rainfall fields over and downstream the lake areas (Song et al., 2004; Sun et al., 2014). All of these research concerns have pointed to the issue that due to the absence in the representation of lake hydrodynamics, the current applications of 1-D lake models to the large deep lakes over TP would suffer from inevitable degraded performances in simulating the lake thermodynamics and their impacts on regional climate.

Recent studies based on the high-resolution remote sensing data have revealed that the Qinghai Lake, Lake Siling Co, and LNC are characterized by large surface areas and complex bathymetry/geometry, and they all exhibit apparent spatial variability in surface water temperature (Ke and Song, 2014; Lu et al., 2019; Xiao et al., 2013), which reflect the interactions between the thermohydrodynamics of large lakes and the overlying atmosphere. Hence, to reveal much more detailed thermal

structures of these TP lakes, we should adopt 3-D hydrodynamic models rather than the most commonly used 1-D lake models, i.e. the Hostetler-based lake component from WRF (WRF-Lake) that has been widely applied for offline/coupled studies on TP lakes (Xu et al., 2016; Zhu et al., 2017; Zhang et al., 2018; Huang et al., 2019; Wu et al., 2019). Based on the valuable 1-yr in-situ water temperature records of LNC, the second largest lake in central TP, the main goals of this study are: (1) to explore the superiority of the 3-D hydrodynamic lake model based on the Princeton Ocean Model (POM) in reproducing the large-lake thermodynamics during May-December than the 1-D WRF-Lake model; (2) to present the 3-D evolution features of thermal structures and hydraulic currents in LNC for the first time. Main findings of this study may help to explain the present shortcomings in the 1-D lake modeling and could provide valuable backgrounds for fully coupling 3-D lake models with atmospheric models to reveal the lake-air interactions over the large lakes of TP.

The rest of this paper is organized as follows. In Section 2, we describe the forcing and validation datasets, the configurations of POM and WRF-Lake, numerical experimental design, and the methodology used in this study. Model comparisons in reproducing the lake surface temperature and water temperature profile are systematically analyzed in Section 3.1. Section 3.2 presents the detailed 3-D thermal structure and circulations in LNC. Finally, summary and discussion are given in

Section 4.

2. Datasets, Model Description and Experimental Design, and Methodology

2.1 Datasets

LNC situates at the northeastern edge of the elevated Nyainqentanglha Mountain, central TP (Figure 1a). It extends from 30°30′N to 30°55′N and 90°16′E to 91°03′E, and has a large surface area exceeding 2000 km^2 and a maximal depth of 98.9 m in its central basin (Wang et al., 2009, 2019). In 2013, two sets of in-situ observations of weather conditions and the lake water temperature profiles were made and these data are used for model initialization and assessments. The daily meteorological variables, i.e., the surface solar radiation, surface downward longwave radiation, relative humidity at 10 m above ground, air temperature at 2 m above ground, and surface pressure and wind speed were collected by an automatic weather station located approximately 1.5 km from the southeastern shoreline of LNC (red aster in Figure 1b). The daily lake water temperature profile, sampled at depths of 3, 6, 16, 21, 31, 36, 56, 66, and 83 m, was measured at the site indicated by the purple aster in Figure 1b (Lazhu et al., 2016). In addition, the MODIS product (MOD11A1), with a spatial resolution of 1 km, provides the instantaneous remote-sensing lake surface temperature (LST) imagery at approximately 11:00 and 21:00 local time over LNC (available at https://modis.gsfc.nasa.gov/data/dataprod/mod11.php; Wan et al., 2004).

The model simulations cover 1th May to 31th December 2013. The atmospheric

forcing inputs include the air temperature at 2 m height, surface pressure, specific humidity and wind speed at 10 m height, and surface downward shortwave and longwave radiation. These input data are mainly derived from the long-term (1979-2018) China Meteorological Forcing Dataset (CMFD) with a temporal resolution of 3 hours and a horizontal resolution of 0.1° (available at http://en.tpedatabase.cn/portal; He et al., 2020). CMFD is produced through assimilating vast amounts of ground-based observations besides several remote-sensing and reanalysis datasets, and it is documented to be a superior near-surface meteorological data for land surface process and hydrology researches over China (Chen et al., 2011; Huang et al., 2017, 2019). Comparison with the in-situ weather station data (Figure 2) demonstrates that CMFD can well represent the daily variations of the over-lake meteorological variables except for an overall underestimation of the wind speed, especially during fall-winter (September to December). Following Lazhu et al (2016), the CMFD wind speed is calibrated using the piecewise linear regression relationships between the daily CMFD and in-situ weather station wind speed established for spring-summer (May to August) and fall-winter, respectively (Figure 2e). The wind direction, which is not available in CMFD, is derived from the contemporarily up-to-date hourly ERA5_Land reanalysis with a horizontal resolution of 9 km (available at https://cds.climate.copernicus.eu; Copernicus Climate Change Service 2019).

2.2 Model Description and Experimental Design

The 3-D coastal ocean model POM solves nonlinear governing equations of lake water motions based on hydrostatic and Boussinesq approximations using finite difference method (Blumberg and Mellor 1987). The horizontal space is discretized with a uniform grid spacing of 1 km, and the vertical discretization uses 31 terrain-following sigma levels with finer resolution near the surface/bottom. The centers of the sigma levels are located at -0.0005, -0.002, -0.0055, -0.009, -0.0155, -0.026, -0.0365, -0.047, -0.0575, -0.068, -0.0785, -0.089, -0.0995, -0.11, -0.1205, -0.131, -0.1415, -0.152, -0.1625, -0.173, -0.1835, -0.194, -0.2045, -0.262, -0.3715, -0.486, -0.6, -0.714, -0.883, -0.9975. The Mellor and Yamada (1982) level 2.5 turbulence closure scheme (MY-2.5) and the Smagorinsky eddy parameterization with a multiplier of 0.2 are employed to calculate the vertical and horizontal mixing coefficients, respectively. The lake water has no exchange of heat with the closed lateral boundaries and lake bottom. The velocity is free-slip along the lateral boundaries, and the friction at the lake bottom is parameterized in quadratic form with the drag coefficient calculated according to:

$$C_{db} = \max\left[\frac{\kappa^2}{ln(z_b/z_{0b})^2}, 0.0025\right] \quad (1)$$

where $\kappa = 0.41$ is the von Karman constant, z_b is the distance from the bottom to the bottom layer center, and $z_{0b} = 0.01\ m$ is the bottom roughness length.

Time-independent forcing is applied at lake surface. The downward shortwave radiation ($SW_{\downarrow}$) and longwave radiation ($LW_{\downarrow}$) are specified according to CMFD, and 40% (60%) of the shortwave radiation are accounted by the infrared (visual) band, with the vertical extinction coefficient assumed as 2.85 (0.1) m^{-1}. The surface wind stress is calculated according to:

$$(\tau_x, \tau_y) = \rho_a C_d (u, v)\sqrt{u^2 + v^2} \quad (2)$$

where τ_x, u (τ_y, v) are the east-west (north-south) component of surface wind stress ($N \cdot m^{-2}$) and wind speed at 10 m height (ms^{-1}), $\rho_a = 100P_a/R_a(273.15 + T_a)$ is the moist air density ($kg \cdot m^{-3}$), P_a is the input surface air pressure (hPa), $C_d = (7.5 + 0.67\sqrt{u^2 + v^2}) \times 10^{-4}$ is the wind drag coefficient (Garratt, 1977). The upward longwave ($LW_{\uparrow}$), sensible ($SH_{\uparrow}$) and latent ($LH_{\uparrow}$) heat fluxes are calculated based on the prognostic water surface temperature. The dynamic lake-air interactions are included in the computed heat fluxes, and this has advantages over the prescribed or precomputed surface heat fluxes (Xue et al., 2015). The equation for $LW_{\uparrow}$ and the bulk aerodynamic formulae for SH and LH (Verburg and Antenucci 2010) are:

$$LW_{\uparrow} = \varepsilon \sigma T_w^4 \quad (3)$$

$$SH_{\uparrow} = \rho_a C_{pa} C_{sh} (T_w - T_a)\sqrt{u^2 + v^2} \quad (4)$$

$$LH_{\uparrow} = \lambda_v \rho_a C_{lh} (q_w - q_a)\sqrt{u^2 + v^2} \quad (5)$$

where $\varepsilon = 0.98$ is the lake surface emissivity, $\sigma = 5.67 \times 10^{-8}\, W \cdot m^{-2} \cdot K^{-4}$ is the Stefan-Boltzmann constant, T_w (T_a) (in K) is the surface water (air) temperature, $R_a = 287(1 + 0.608q_a)$ (in J·kg^{-1}·K^{-1}) is the gas constant for moist air, $C_{pa} = 1005$ J·kg^{-1}·K^{-1} is the specific heat of air, $C_{sh} = 0.0001$ ($C_{lh} = 0.00016$) is the bulk constant coefficient of sensible (latent) heat, $\lambda_v = 2.501 \times 10^6 - 2370(T_a - 273.15)$ is the latent of vaporization, and q_a (q_w) (in kg·kg^{-1}) is the (saturated) specific humidity. For all the above heat flux components, positive (negative) values mean that the lake water loses (gains) heat from the atmosphere.

The version of POM used for the present study does not include an ice component. Hence, the simulation is carried out from 1th May 2013 to 31st December 2013 to avoid dealing with the season with significant ice cover from January to April (Gou et al., 2017). POM is initialized with zero currents, a constant salinity of 1.7g L^{-1}, and a uniform temperature of 1.96°C, which is the depth-averaged value of the rather homogeneous lake water temperature at 1th May 2013 according to in-situ observations.

Besides POM, the 1-D lake component in the Weather Research and Forecasting Model (WRF-Lake), which solves the snow, lake water/ice, and soil sediment processes within a lake column, is also used. Detailed model descriptions can be found in Gu et al. (2015). WRF-Lake has undergone significant model process calibrations and has been

282 extensively applied in simulating the lake thermodynamics for various offline/coupled
283 applications (Huang et al., 2019; Wang et al., 2019; Wu et al., 2019, manuscript
284 submitted to *Clim. Dyn*; Xu et al., 2016). In this study, the 1-D WRF-Lake with 25
285 vertical lake layers is solved for each horizontal grid of POM for the same 8-month
286 period. Using the same initial conditions and surface forcing as used by POM, 1-D
287 WRF-Lake gives a 3-D thermal representation of LNC for comparison with the POM
288 simulation. Additionally, we conducted a series of sensitivity experiments and
289 introduced adjustments to several key parameters, i.e. a parameterized surface
290 roughness length (Subin et al., 2012), realistic temperature of maximum water density
291 (Tdmax=3.5^{o}C), and a decreased light extinction coefficient with a scale factor of 0.8,
292 to obtain the optimal WRF-Lake results for comparison.

293 **2.3 Methodology**

294 For comparisons with the in-situ observations, the lake temperature profiles
295 simulated by POM and WRF-Lake at the observation site are selected and linearly
296 interpolated onto the observed layers. The bimonthly MODIS and model simulated
297 LST are processed following two steps. First, for each MODIS imagery, the values on
298 the pixels located within the lake model domain (Figure 1b) are extracted. Because
299 POM does not contain an ice component, the nearshore MODIS pixels with LST
300 values less than 0°C are excluded. Second, the selected MODIS data are interpolated
301 onto the model grids with the bilinear interpolation method (Shepard 1968). The

gridded MODIS LST can then be compared with the model results at bimonthly intervals. The assessment uses four statistical parameters, i.e., the mean bias (BIAS), root-mean-square error (RMSE), Pearson temporal correlation (TC), and the Taylor score (TS), following Huang et al (2019).

The heat balance for the lake water column in a given time interval can be expressed as (Wetzel and Likens 2000; Titzel and Austin 2014):

$$\frac{\delta}{\delta t} LHC = SNHF + \theta_{hor} + \theta_{sed} \tag{6}$$

$$LHC = C_{pw}\rho_w \int_0^h T(z)dz \tag{7}$$

$$SNHF = SW_{\downarrow} + LW_{\downarrow} - LW_{\uparrow} - SH_{\uparrow} - LH_{\uparrow} \tag{8}$$

where $\delta LHC/\delta t$ (W·m^{-2}) is the rate of heat content change within the lake column of unit area, which is balanced by the surface net heat flux ($SNHF$, W·m^{-2}), horizontal heat transport due to advection and mixing (θ_{hor}, W·m^{-2}), and the conductive heat exchange between lake water and bottom sediments. $C_{pw} = 4180$ J·kg^{-1}·K^{-1} is the specific heat of water, $\rho_w = 1000$ kg·m^{-3} is the water density, h is the bottom lake depth, $T(z)$ (in ^{o}C) is the lake temperature at depth z (in m). Note that $\theta_{hor} = 0$ for the 1-D WRF-Lake model, and can be estimated as $\delta LHC/\delta t - (LHC + SNHF)$ in POM due to the adiabatic bottom boundary conditions. Positive $SNHF$ and θ_{hor} mean that the lake column gains heat. The above heat budget components are firstly

calculated based on the daily POM results and are then analyzed for bimonthly intervals for representations. The heat budget analysis is not performed for November-December due to the missing solution of ice thermodynamics in POM.

3. Results

3.1 Model Comparisons: Surface Layer Temperature and Lake Water Temperature Profile

3.1.1 Surface Layer Temperature

Figure 3 gives the in-situ observed and simulated daily time series of the lake temperature at 3-m depth ($TLake_{3m}$), and Figure 4 presents the related quantitative statistics at both daily and bimonthly timescales to evaluate the abilities of POM and WRF-Lake in reproducing the lake surface layer temperature. Since 1th May 2013, the $TLake_{3m}$ at the Nam Co buoy exhibits a continuous warming tendency from 2^{o}C to 11.9^{o}C until late August and then gradually decreases to 1.35 ^{o}C at the end of December (Figure 3). Although both POM and WRF-Lake generally reproduced the daily $TLake_{3m}$ variability with the TC/TS exceeding 0.95 (Figure 4), the 3-D lake model POM shows preferable capabilities in the temporal evolution of $TLake_{3m}$ during May-December. Specifically, POM gives better representations in the rapid lake warming process since early June, the gradual $TLake_{3m}$ decrease during the autumnal destratification period, and the synoptic cooling events under weak lake stratification around mid-December, suggesting that POM can reasonably capture the

337 lake physical processes on seasonal and synoptic timescales. The 1-D WRF-Lake
338 tends to underestimate the $TLake_{3m}$, especially for the lake
339 destratification/overturning periods with the large negative BIAS of -1.74 (-1.45) ^{o}C in
340 September-October (November-December), while the $TLake_{3m}$ simulated by POM
341 shows a slight warm BIAS (RMSE) of 0.2 (0.52) ^{o}C for the whole simulation period
342 (Figure 4).

343 Figure 5 gives the spatial distribution of the bimonthly MODIS observed and
344 POM/WRF-Lake simulated LST. Figures 6 and 7 present the bimonthly variations of
345 heat budgets ($\delta LHC/\delta t, SNHF, \theta_{hor}$) simulated by POM over LNC and at the Nam
346 Co water temperature site, respectively. With the intensified solar heating in
347 May-June, LNC experienced the springtime warming process from its original
348 thermally mixed state in pre-winter. The simultaneous lake column heat storage shows
349 a general increase across the whole lake (Figure 6a). As the depth-influenced heat
350 capacity increases from coastal to central lake regions, LST over the shallower areas
351 rises with a faster rate in response to the radiative forcing. The horizontal
352 nearshore-offshore temperature gradient forms basically across the isobath (Figures
353 5a-c), which is also documented in many other large deep lakes with sloping bottom
354 bathymetry (Bai et al., 2013; Rao et al., 2004). This cross-isobath temperature
355 gradient can not only enhance the horizontal temperature diffusion, but also stimulate

356 the vertical shear of the water flow through the thermal wind relation to form
357 density-driven movements, both of which tend to redistribute the water/energy within
358 the lake (Beletsky and Schwab 2001). During May-June, the surface currents in LNC
359 consist of two contour-rotating gyres in response to the baroclinic and bathymetry
360 effects (Figure 5b). As the cyclonic circulation in the main basin sustains the heat
361 advection from the warm shore to the mid-lake areas (Figure 6c), the LST pattern
362 simulated by POM is characterized by a less pronounced nearshore-offshore
363 temperature gradient, and thus the 'cold pool' in the central deep lake is warmer than
364 the 1-D WRF-Lake results (Figures 5b and c). At the Nam Co water temperature site,
365 the horizontal heat exchanges contributes approximately 12% of the bimonthly
366 increase rate in lake column heat storage (Figure 7), illustrating that the resolved
367 flow-dependent heat transport plays an important role in POM for reproducing the
368 more realistic LST warming strength during May-June relative to the 1-D WRF-Lake
369 simulations. Accompanied by the persistent solar radiation heating and the
370 water/energy transportation toward the basin center during July-August, the spatial
371 variability of LST decreases and LNC gets fully stratified with a relatively
372 homogeneous epilimnion (as seen for instance in the July-August plot of Figure 9).
373 Lake circulations are dominated by anticyclonic motions in the eastern small basin
374 and appear as regional cyclonic gyres in the main basin due to the stratification
375 development (Figure 5e). Such hydrodynamic processes maintain the summertime

energy transport from heat surplus to colder deep regions and decrease the spatial variabilities of LHC change (Figures 6d-f). During July-August, the horizontal heat exchanges account for ~14% of the increase in lake column heat content at the in-situ station and favor for the satisfactory LST warming simulation by POM (Figures 3 and 7). In comparison with the bimonthly lake-averaged LST from MODIS products, both POM and WRF-Lake overestimate with a BIAS of 0.28 (0.83) ^{o}C and 0.3 (0.27) ^{o}C during May-June (July-August), respectively (Table 1). As reported by previous MODIS LST evaluation researches, the remote-sensed LST from satellites is usually lower than the in-situ measurements due to the cool skin effects, and the absolute BIAS against many other lake field observations is within the range of 0.8-1.9°C (Hook et al., 2003; Ke and Song 2014). Hence, we consider that both models exhibit good performances in qualitatively reproducing the lake-averaged LST during the spring-summer periods. However, the models' abilities in simulating the synchronous LST spatial distributions are hard to evaluate because the model BIAS and data uncertainties possess comparable magnitudes.

Driven by the strong winds and large positive lake-air temperature and humidity gradients during September-October, the over-lake turbulent sensible/latent heat fluxes increase rapidly and act a negative feedback on LST. The lake-averaged LST from MODIS (POM) experienced comparable cooling amplitudes from 10.74 (11.57)

395 °C in July-August to 9.38 (9.85) °C in September-October (Table 1). While, the
396 simultaneous LST modeled by WRF-Lake shows an excessive decrease of 2.79°C from
397 11.01°C to 8.20°C, which has been previously reported as the rapid autumnal cooling
398 issue in Hostetler model by Martynov et al (2010). LST from both MODIS and POM
399 presents a pronounced horizontal gradient increasing from northwest to southeast
400 (Figures 5g and h), which can be partly attributed to the eastward warm water
401 aggregation caused by the prevailing westerly wind, especially during October when
402 the lake circulation is largely influenced by the surface winds under weakly stratified
403 conditions (not shown). However, such LST spatial pattern cannot be well captured by
404 the 1-D WRF-Lake model, implying that the hydrodynamic processes besides the local
405 turbulent lake-air fluxes must be considered for redistributing energy and better
406 simulating the LST spatial variability over large deep-water bodies such as LNC.
407 During September-October, the horizontal energy transportation is basically from the
408 western coastal to central lake regions (Figures 6g-h). For the Nam Co water
409 temperature site, the eastward energy transport during this period tends to counteract
410 the significant $SNHF$ loss and leads to the more realistic decrease rate of LST modeled
411 by POM compared to the 1-D WRF-Lake simulations (Figures 3 and 7). With the
412 progress of destratification and overturning processes during autumn-winter, the entire
413 water body temperature descends continuously with a slower LST decreasing rate over
414 central deep water regions, where the epilimnetic heat loss can be partly compensated

by the warm hypolimnion due to the wind-induced mixing or gravitationally-driven vertical energy exchanges when the LST decreases to Tdmax. From MODIS products, LST in the middle lake is approximately 1.5^{o}C higher than that in the coastal areas during November-December. Although both models present a warmer LST in middle lake, the lake-averaged LST simulated by WRF-Lake is unrealistically lower than the MODIS LST with a large BIAS of -2.6 ^{o}C. The excessive LST decrease in the 1-D WRF-Lake model can be attributed to the insufficient upward heat transport induced by the unresolved Ekman upwelling and the less heat retention in the central lake regions during previous spring-summer periods (Figures 5j-i). For the autumn-winter periods, POM is evidently superior in modeling both the lake-averaged LST with much lower BIAS/RMSE and the spatial distribution of LST compared with the WRF-Lake simulations.

3.1.2 Vertical Temperature Profile

In this section, we assessed the seasonal variation of vertical temperature profile modeled by POM and WRF-Lake against the field mooring observations. Figure 8 presents the time-depth distributions of the daily observed and modeled water temperature during May-December, and Figure 9 quantitatively evaluates models' performance in simulating the lake temperature at 10 observed layers. To indicate the development of lake thermal stratification, we define the first/last date, from which the

434 temperature differences between 6-m and 66-m lake depth are greater than 1^{o}C, as the
435 onset/end of lake thermal stratification (Wang et al., 2019).

436 From Figure 8a, the observed water column at the Nam Co buoy shows a small
437 negative temperature gradient from the lake surface to deeper layers until the lake
438 thermal stratification establishes at 4th June. As the result of the persistent radiative
439 heating during June to late September (Figures 2a and b), the vertical thermal
440 structure at this deep-water station is characterized by a rather homogeneous warm
441 epilimnion with its maximum depth exceeding 30m. Since then, the mean epilimnetic
442 temperature gradually descends to ~5.5^{o}C due to the intensified surface heat flux loss
443 and vertical mixing strength, and the mixed layer depth finally reaches ~50m at the
444 end of destratification period (7th November). During the subsequent lake overturning
445 periods, the entire water body temperature experiences an almost uniform cooling
446 process before the LST approaches the Tdmax around mid-December, after which the
447 typical inverse thermal stratification begins to develop due to the density-driven
448 convection.

449 Both POM and WRF-Lake can generally reproduce the seasonal evolution of
450 thermal structures, especially for the pattern and amplitude of the subsurface (3-16m)
451 water temperature variability implied by the TC/TS greater than 0.9 (Figures 9a and c).
452 However, their capabilities in quantitatively simulating the stratification development

vary significantly and several discrepancies against field measurements are evident. First, the establishment of thermal stratification modeled by POM (7thJune) and WRF-Lake (15th June) is somewhat postponed than the observations (4th June). POM predicts the onset of stratification more accurately because the flow-dependent heat transport from warm nearshore areas to Nam Co station is beneficial for an earlier stratification development (Figure 6c and 7). Second, both models show degraded performances in modeling the temperature of metalimnion, and the largest discrepancies occur at the 21-m lake depth with a much smaller RMSE of 1.3^{o}C from POM than from WRF-Lake (2.38^{o}C) (Figure 9b). In terms of the oscillating evolution of thermocline displacements, POM also performs better than WRF-Lake despite with some errors. For example, the mixed layer in POM is shallower and the thermocline is more diffuse compared with the observations, which is consistent with the similar issue reported by the previous POM applications on Lake Michigan and Lake Erie (Beletsky et al., 2006, 2013). Additionally, during the late summer, POM fails to capture the rapid thermocline jump episodes occurring at 21-31m, where the short-term temperatures were documented to exhibit large abrupt fluctuations exceeding 3^{o}C due to the intensive internal wave activities in the upper portion of thermocline (Wang et al., 2019). These discrepancies,which can be attributed to both the wind fields uncertainties and the current POM model's intrinsic defects including the absent nonbreaking wave-induced mixing (i.e. Langmuir circulation), the numerical diffusion,

and the not fully resolved internal waves (Huang and Qiao, 2010; Kantha and Clayson 2004), are still challenging problems to overcome. Third, the destratification date modeled by WRF-Lake (31th October) is earlier than the observation (7th November), while it is delayed by about 2 weeks in the POM results (20th November). As previously discussed in explaining the LST underestimation by WRF-Lake during autumn-winter periods, the modeled earlier autumnal destratification and colder wintertime water column temperature at this deep-water station are also the results of the less heat retention and the missing horizontal energy exchanges. The postponed destratification in POM points to the issue again that the current wind-wave-induced mixing strength in POM is insufficient to describe the convection activities under both the strong and weak stratified phases. This concern needs to be remedied before its coupling application on exploring the ecological impacts of lake thermal stratification.

In summary, the 3-D POM shows much better ability than the 1-D WRF-Lake in reproducing the seasonal and synoptic variations of LST and vertical thermal structures. The RMSEs of the POM modeled water temperature at all of the 10 observed layers are within a reasonable range from 0.39°C to 1.3 ^{o}C (Figure 9b). This gives us confidence to present the 3-D thermal structure and circulations of LNC in the following Section.

3.2 Three-Dimensional Thermal Structure and Circulations

As documented by previous studies, the temperature fields and current structure in large lake water bodies show pronounced spatiotemporal variability due to the multiscale thermohydrodynamics (Nyamweya et al., 2016; Xue et al. 2015, 2017). LNC is a large typical dimictic lake and features complex limnological phenomena during May-December, i.e. spring thermal bar, summertime stratification, autumnal destratification, and hibernal turnover processes (Wang et al., 2019), all of which significantly affect the natural/anthropogenic particle transport and the biota growth within the lake ecosystems. To broaden the knowledge about the thermodynamics of LNC from limited in-situ observations, we are going to utilize the POM results to obtain more specifics about the development of the 3-D lake thermal structure and circulations in the following part. Figures 10 and 11 present the lake temperature along a vertical southwest-northeast transection, the LST, and the depth-averaged water currents at monthly timescales.

For many large temperate lakes with sloping bottom bathymetry, the spring thermal state is mainly determined by an important limnological phenomenon namely "thermal bar", which is defined as the water column with the temperature of Tdmax and serves as a barrier in separating the stratified nearshore waters and the thermally mixed central deep water areas (Rao et al., 2004; Tsydenov 2019). The spring thermal bar reflects the thermohydrodynamic processes in response to the radiative heating and

density-driven adjustment when the lake is heated convectively from cold water temperature to Tdmax. The classical spring thermal bar development can also be observed in LNC (Figures 10a and b). Firstly, due to the high altitude (4731m) and the related cold air temperature over LNC during winter, the lake water temperature is usually rather homogenous with a value less than 2^{o}C before May. Such a low heat retention in previous winter provides the essential prerequisites for the spring thermal bar development. As the result of the intensified solar radiation from spring to early summer and its depth-decayed penetrating features (Figures 2a and b), the upper water body receives large portions of the incoming radiation and is heated towards Tdmax. During this period, the denser epilimnion would continuously sink and mix with the cold deeper water body, and thus the whole lake column temperature rises homogeneously with a slow rate until the hypolimnetic temperature reaches Tdmax and the stable density gradient forms. From then on, the epilimnetic temperature rises rapidly due to the weakened top-to-bottom mixing, as can be indicated by the fast $TLake_{3m}$ warming tendency at the Nam Co buoy since the onset of thermal stratification (4th June) (Figures 3 and 8). A weak thermal stratification is firstly established around the coastal regions of LNC in May, while the deep mid-lake regions still experience the convective heating process due to the larger heat capacities (Figure 10a). There exists a narrow zone with typical converging flow patterns (namely thermal bar), which divides the warm stratified nearshore and cold thermally homogeneous

offshore areas and inhibits the horizontal water/energy exchanges between them. During this period, as the thermal bar hasn't reached the deep-water Nam Co buoy (~93m), its water column is mainly characterized by the continuous gravitationally-driven convection in response to the density inversion triggered by radiative heating. Hence, the water coulumn temperature at this station exhibits a slow warming tendency (Figure 8) and the observed (POM modeled) $TLake_{3m}$ rises weakly from 1.99 (1.99) ^{o}C to 3.44 (3.21) ^{o}C during May (Figure 3). While, once the thermal bar passes across the Nam Co buoy during its progressive movement from shoreline to the deep mid-lake parts, the $TLake_{3m}$ rises rapidly due to the weakened top-to-bottom mixing and the horizontal heat transport from warm nearshore regions (Figures 3 and 6c), implying the establishment of thermal stratification at this water temperature site (4^{th} June as observed). POM gives a reasonable simulation in the onset of the stratified phase at this in-situ site (7^{th} June) and reveals that the thermal stratification in the central deep-water regions builds up approximately one month later than that occurs in the nearshore areas. This is consistent with the conclusion from Wang et al (2019) by comparing the in-situ water temperature records at two stations located at the main basin and the eastern small basin, respectively.

According to the POM results, the summer thermal stratification is basically established over LNC when the spring thermal bar eventually arrives at the mid-lake

area and vanishes around 10th June (not shown). From May to June, the isobath-following temperature pattern still exists but becomes less pronounced as the consequence of the horizontal basin-scale water/energy exchanges, indicating the important effects of gyre-related hydrodynamics on large-lake thermal states. The lake-averaged LST increases from 3.17 ^{o}C to 7.7 ^{o}C (Figures 10b and d). In contrast to the weak depth-averaged water flow reaching a few cm s^{-1} in May, the mean lake current in June increases in magnitude and is featured by two organized contour-rotating gyres in geostrophic balance with the density fields (Figure 10d). The density-driven circulation in the central deep regions is cyclonic and the thermocline has a distinctive dome shape, resembling that in the deeper basin of Lake Michigan and Lake Erie (Beletsky and Schwab 2008; Beletsky et al., 2013). The eastern small basin is characterized by an anticyclonic circulation and a bowl-shaped thermocline. The two basin-scale gyres in June still remain the dominant monthly circulation patterns in July despite with some discrepancies (Figure 10f). In July, the circulation speed increases slightly with the developing summer stratification, which can be indicated by the deepening and temperature increase of the main thermocline. The enhanced cyclonic flow in the main basin further generates evident mid-lake upwelling due to the upward Ekman transport, resulting in the thermocline's dome shape. In August, the gyration features of the depth-averaged currents become less pronounced and the strength of mid-lake upwelling gets weaker, failing to maintain the domed thermocline (Figures

10g and h). The lake circulation, especially over the top mixed layer, is likely influenced by the surface winds and characterized by a long nearshore flow along the northwestern coastal regions, which significantly modifies the thermal structures in the upper water body (Figure 10g). On one hand, as the warm water is advected following the nearshore currents, the monthly mean LST in August exhibits a northwest increasing trend different from the isobath-following LST pattern in May-July. On the other hand, the prevailing offshore (onshore) currents can produce the upwelling (downwelling) events and thus lead to the upward (downward) curved isotherms around 90.82°E (90.35°E) (Figures 10g and h). Overall, from June to August, the thermal stratification of LNC is in its developing phase and the monthly lake-averaged LST exhibit a stepwise increase from 7.7^{o}C in June to 10.75^{o}C in July and 12.07^{o}C in August.

Since September, LNC begins to lose vast net energy and enters the autumnal destratification period due to the decreased net radiations, enhanced over-lake wind, and the large positive lake-air temperature/humidity gradients (Figure 2). From August to September, the lake-averaged LST decreases from 12.07^{o}C to 10.88^{o}C. The depth-averaged currents in September is rather lower with near-zero flow speeds in the central open-water regions (Figure 11b). There exist two weak anticyclonic gyres in the southwestern corner around (30.65°N, 90.5°E) and the eastern small basin, which may

589 be induced by the residual negative current vorticity from previous months. The
590 simultaneous epilimnion shows a slight deepening and the top thermocline possesses
591 bowl shapes across the lake (Figure 11a). Since October, the large-scale 500-hPa wind
592 fields over TP (Maussion et al., 2013) and the local surface winds over LNC both
593 exhibit significant enhancements in their westerly components. As a result, the
594 eastward water currents pick up in speed and transport warm mixolimnion water to the
595 southeastern part of LNC in October. The mixed layer is tilted eastward and the spatial
596 distribution of LST is characterized by a southeast increasing gradient (Figures 11c and
597 d). From September to October, the lake-averaged LST decreases from 10.88^{o}C to
598 8.57^{o}C. In particular, at the end of October, the bowl-shaped mixolimnion at the
599 deep-water Nam Co buoy can deepen to ~30m and the metalimnion is widely
600 distributed across the 30-60m, which supports the remarkable increases (~2^{o}C) of the
601 observed/modeled 31-m, 36-m, and 56-m water temperature during this period (Figures
602 8a and b). Similarly, the wind-induced deepening of mixolimnion/metalimnion would
603 lead to the abrupt increase (~1.5°C) in the 66-m and 83-m water temperature at this
604 station in early November.

605 In November, lake circulation shows a general increase in speed and features a
606 cyclonic flow in the main basin due to the persistent mechanical energy transportation
607 from surface westerlies (Figure 11f). This suggests the common effects of wind forcing

608 and bathymetry on water currents. The lake-averaged LST in November decreases to
609 5.34^{o}C and the thermal stratification greatly weakens (Figure 11e). It is worth noting
610 that the water column in the western coastal regions exhibits a faster destratification
611 speed due to the eastward heat transportation. LNC begins to stratify around 7th
612 November and the whole lake is thermally mixed again on 26th November according to
613 the POM modeled daily evolution of thermal structures. Given that POM gives a
614 postponed prediction in the destratification date at Nam Co buoy (20th November
615 versus observed 7th November), the actual total destratification date for LNC is
616 speculated to be around mid-November. Since then, when the LST gradually
617 decreases to Tdmax in December, a typical autumn thermal bar forms in the coastal
618 regions first and moves progressively toward the lake center (Figure 11g), causing the
619 LNC to enter into the overturning period. From POM results, the autumn thermal bar
620 lasts for approximate one month, comparable to the lifetime of spring thermal bar, and
621 eventually vanishes at the mid-lake regions around 26th December. Then the thermal
622 state in LNC is mainly characterized by an inverse and weak wintertime stratification.
623 At the monthly mean timescale, LST in December exhibits a negative
624 nearshore-offshore temperature gradient and the lake-averaged LST decreases to
625 2.64^{o}C (Figure 11h). The wind-induced lake circulation features a pronounced cyclonic
626 vorticity in the main basin, which gives rise to the upward movement of warm
627 hypolimnion and works in concert with the gravitationally-driven convection to

strengthen the top-to-bottom mixing during the overturning period.

4. Summary and Discussion

In this study, with the guidance of both the valuable 1-yr in-situ water temperature records and the satellite observations during May-December 2013, we explored the performances of the 3-D POM and 1-D WRF-Lake in reproducing the thermal structures of LNC, the second largest lake over central TP. Moreover, we also present detailed discussions about the monthly development of 3-D lake thermodynamics and related circulation patterns based on POM simulations. Main findings are summarized as follows:

Both models can well reproduce the daily evolution of the observed $TLake_{3m}$ at the deep-water buoy (~93m) in LNC, with the TC/TS exceeding 0.95. In terms of the magnitude, WRF-Lake tends to underestimate $TLake_{3m}$, especially during fall-winter periods (September-December). However, POM exhibits preferable capabilities in reproducing the rapid $TLake_{3m}$ increase since June, the gradual $TLake_{3m}$ decrease during destratification/overturning period, and the transient $TLake_{3m}$ oscillating events around mid-December, suggesting that the hydrodynamic POM is more reasonable in capturing the seasonal and synoptic response processes of lake temperature to the regional atmospheric conditions. The BIAS (RMSE) of the modeled $TLake_{3m}$ during May-December is improved from -1.05°C (1.26°C) in WRF-Lake to

0.2°C (0.52°C) in POM.

Meanwhile, POM also performs better than WRF-Lake in reproducing the spatial distribution of bimonthly LST, which emphasized again that the complex temperature-current interactions must be considered for reasonably reproducing the spatial variability of LST over large TP lakes. For example, during the spring-summer warming periods (May-August), LST is mainly characterized by a persistent nearshore-offshore gradient due to the differential heating mechanism (Monismith et al., 1990), where shallower coastal regions with smaller heat capacity warms faster in response to the intensified radiative heating. This cross-isobath temperature gradient could last for several months and tend to transport vast energy to the mid-lake heat deficit regions through both enhanced thermal diffusion and geostrophic balanced water flows (Beletsky and Schwab 2008; Song et al., 2004). However, as the lake thermodynamics in WRF-Lake is simplified as just vertical with no horizontal water/energy exchanges, the modeled LST is featured by excessively warm shorelines and a pronounced central 'cold pool' (Figures 3c and f). The modeled lake temperature at the deep-water Nam Co buoy shows inadequate summertime warming strength and the thermal stratification builds up later than the observation (15th June versus the observed 4th June). Additionally, the missing flow-dependent water/energy transport in WRF-Lake leads to smaller mid-lake heat storage during May-August

than that in observation or POM simulations, as implied by the metalimnion (16-36m) temperature (Figure 8). The less heat retention simulated by WRF-Lake would further work with its unresolved upward Ekman heat transport to jointly contribute the significant LST underestimation during fall-winter (September-December). At the Nam Co water temperature station, WRF-Lake underestimates the autumnal lake column temperature with a distinct shallower and much colder mixed layer, leading to the earlier destratification (31th October versus 7th November in observation) and the onset of wintertime inverse thermal stratification.

Model intercomparison indicates that both the local lake-air feedbacks and the heat redistribution processes related to the lake thermohydrodynamics should be considered for better representing the spatiotemporal variability of LST and the vertical thermal structures. This is also of great necessities for researching the development of important limnological phenomena and their ecological impacts. With the guidance of in-situ water temperature records and previous observation work over LNC, we give a first-step discussion about its monthly 3-D thermal structure and circulations based on POM results. The springtime overturning processes of LNC occur from 1th May to 10th June 2013, during which typical thermal bar form in the coastal region first in response to the density instabilities triggered by penetrating radiative heating, and then moves progressively towards the center LNC. The thermal

685 stratification builds up around early June and develops with deepening
686 mixolimnion/thermocline during summer (June-August), with the lake-averaged LST
687 increases from 7.7°C to 12.07°C. In terms of the summer lake circulation, the
688 depth-averaged currents in the main basin (eastern small basin) exhibits a cyclonic
689 (anticyclonic) gyre in geostrophic equilibrium with the density fields. The
690 thermocline in the eastern small basin possesses a bowl shape throughout summer,
691 while the top thermocline in the main basin features dome shapes in June-July and
692 bowl shape in August because the epilimnetic water flow experiences a
693 transformation from cyclonic gyre to pronounced long nearshore currents. Since
694 September, LNC enters the autumnal destratification period and is speculated to be
695 thermally mixed again around mid-November due to the decreased solar radiation and
696 significant surface net heat flux loss. With the LST further decreases to Tdmax, the
697 autumnal thermal bar develops in the western part of LNC first and gradually turns
698 over the whole water body until the wintertime inverse thermal stratification basically
699 builds up around mid-December. The lake circulation during October-December is
700 characterized by eastward water flow or a dominant cyclonic gyre in the main basin,
701 which can be attributed to the interplay between prevailing surface westerlies and lake
702 bathymetry.

703 At present, there still exist some aspects to be improved for expanding POM's

applicability in researching the lake thermal evolution of LNC or other large deep lakes over TP. First, for the deep-water Nam Co buoy, the modeled mixed layer depth is shallower and the destratification date is delayed about two weeks, implying that the vertical mixing strength is underestimated due to the lacking of nonbreaking wave-induced mixing in current POM. Possible remedies are to implement the MY-2.5 turbulence closure scheme with a wind-wave-induced parameterization (Hu and Wang 2010; Bai et al., 2013) or to couple with a surface wave model, i.e. WAVEWATCH III (Tolman 2009). Additionally, as most TP lakes possess long-lasting ice-covered periods due to their high-altitude features, it is of great necessity to incorporate an ice component into POM in the future. This is especially important for the ice formation/melting periods when the lake thermohydrodynamics are influenced by both the ice movement and its modifications on lake surface layer properties (i.e. albedo, thermal conductivity, and water salinity).

Acknowledgement. This study is supported by National Natural Science Foundation of China under Grants 41975081, the National Key R&D Program of China under Grant 2017YFA0604301, the Jiangsu University "Blue Project" outstanding young teachers training object, and the Fundamental Research Funds for the Central Universities and the Jiangsu Collaborative Innovation Center for Climate Change. We are grateful to NASA for providing the MODIS LST product (MOD11; available at https://modis.gsfc.nasa.gov/data/dataprod/mod11.php) and the Institute of

Tibetan Plateau Research,Chinese Academy of Sciences (ITPCAS) for providing the China Meteorological Forcing Dataset (CMFD) (available at http://en.tpedatabase.cn/portal). We also appreciate Dr. Junbo Wang and Dr. Lei Huang for providing the station data, which is available at the website http://en.tpedatabase.cn/portal/MetaDataInfo.jsp?MetaDataId=177.

Reference

Aijaz, S., M Ghantous, AV Babanin, I Ginis, B Thomas and G Wake (2017). Nonbreaking wave-induced mixing in upper ocean during tropical cyclones using coupled hurricane-ocean-wave modeling. J. Geophys. Res. Oceans, 122, 3939-3963. Doi: 10.1002/2016JC012219

Ao, YH, SH Lyu and ZG Li (2018). Numerical simulation of the climate effect of high-altitude lakes on the Tibetan Plateau. Sciences in Cold and Arid Regions, 10(5): 0379-0391. Doi: 10.3724/SP.J.1226.2018.00379

Bai, XZ., J Wang, DJ Schwab, Y Yang, L Luo, GA Leshkevich and SZ Liu (2013). Modeling 1993-2008 climatology of seasonal general circulation and thermal structure in the Great Lakes using FVCOM. Ocean Modelling, 65: 40-63. Doi: 10.1016/j.ocemod.2013.02.003

Beletsky, D. and DJ Schwab (2001). Modelling circulation and thermal structures in Lake Michigan: Annual cycle and interannual variability. J. Geophys. Res., 106: 745-771. Doi: 10.1029/2000JC000691

——, JD Schwab and M McCormick (2006). Modeling the 1998-2003 summer circulation and thermal structure in Lake Michigan. J. Geophys. Res. 111, C10010. Doi: 10.1029/2005JC003222

—— and JD Schwab (2008). Climatological circulation in Lake Michigan. Geophys. Res. Lett.,

35, L21604. Doi: 10.1029/2008GL035773

——, N Hawley, YR Rao, HA Vanderploeg, R Beletsky, DJ Schwab and SA Ruberg (2012). Summer thermal structure and anticyclonic circulation of Lake Erie. Geophys. Res. Lett., 39, L06605. Doi: 10.1029/2012GL051002

——, N Hawley and YR Rao (2013). Modeling summer circulation and thermal structure of Lake Erie. J. Geophys. Res., 118, 6238-6252. Doi: 10.1002/2013JC008854

Bennington, V., GA Mckinley, N Kimura and CH Wu (2010). General circulation of Lake Superior: Mean, variability, and trends from 1979 to 2006. J. Geophys. Res., 115, C12015. Doi: 10.1029/2010JC006261

——, M Notaro and KD Holman (2014). Improving climate sensitivity of deep lakes within a regional climate model and its impact on simulated climate. J. Clim., 27: 2886-2911. Doi: 10.1175/JCLI-D-13-00110.1

Biermann, T., W Babel, WQ Ma, XL Chen, E Thiem, YM Ma, and T Foken (2014). Turbulent flux observations and modelling over a shallow lake and a wet grassland in the Nam Co basin, Tibetan Plateau. Theor. Appl. Climatol., 116, 301–316. Doi: 10.1007/s00704-013-0953-6

Blumberg, AF and GL Mellor (1987). A description of a three-dimensional coastal ocean circulation model, three-dimensional coastal ocean circulation model. Three-Dimensional Ocean Models, American Geophysical Union, Washington DC, Chapter 4. Doi: 10.1029/CO004p0001

Blokhina NS and DI Selin (2019). Spring thermal bar formation in a water reservoir with a complex bottom relief (for Lake Ladoga as an example). Moscow University Physics Bulletin, 74(1):58-63. Doi: 10.3103/S0027134919010065

Chen, YY., K Yang, J He, J Qin, J Shi, J Du and Q He (2011). Improving land surface temperature

modeling for dry land of China. J. Geophys. Res., 116, D20104. Doi: 10.1029/2011JD015921

Copernicus Climate Change Service (C3S) (2019). C3S ERA5_Land reanalysis. Copernicus Climate Change Service. Doi: 10.24381/cds.e2161bac

Cui, LB and XY Li (2014). Characteristics of stable isotope and hydrochemistry of the groundwater around Qinghai Lake, NE Qinghai-Tibet Plateau, China. Environ. Earth. Sci., 71: 1159-1167. Doi: 10.1007/s12665-013-2520-y

Dai, YF., L Wang, TD Yao, XY Li, LJ Zhu, and XW Zhang (2018a). Observed and Simulated Lake Effect Precipitation Over the Tibetan Plateau: An Initial Study at Nam Co Lake. J. Geophys. Res. Atmos., 123, 6746–6759. Doi:10.1029/2018JD028330

Dai, YJ., N Wei, AN Huang, SG Zhu, W ShangG, H Yuan, SP Zhang, and SF Liu (2018b). The Lake Scheme of the Common Land Model and its performance evaluation. Chinese Science Bulletin 63(28-29). Doi:10.1360/N972018-00609

Garratt JR (1977). Review of drag coefficients over oceans and continent. Mon. Wea. Rev., 105(7):915-929. Doi:10.1175/1520-0493(1977)105<0915:RODCOO>2.0.CO;2

Gerken, T., W Babel, FL Sun, M Herzog, YM Ma, T Foken and HF Graf (2013a). Uncertainty in atmospheric profiles and its impact on modeled convection development at Nam Co Lake, Tibetan Plateau. J. Geophys. Res. Atmos., 118, 12: 317-331. Doi: 10.1002/2013JD020647

——, T Biermann, W Babel, M Herzog, YM Ma, T Foken, and HF Graf (2013b). A modelling investigation into lake-breeze development and convection triggering in the Nam Co Lake basin, Tibetan Plateau. Theor. Appl. Climatol., 117(1-2):149-167. Doi:10.1007/s00704-013-0987-9

Gill A (1982). Atmosphere-Ocean Dynamics, Academic, New York.

790 Gou, P., QH Ye, T Che, Q Feng, BH Ding, CG Lin and JB Zong (2017). Lake ice phenology of
791 Nam Co, Central Tibetan Plateau, China, derived from multiple MODIS data products. J.
792 Great Lake Res. Doi: 10.1016/j.jglt.2017.08.011

793 Gu, HP., JM Jin, YH Wu, MB EK, and ZM Subin (2015). Calibration and validation of lake
794 surface temperature simulations with the coupled WRF-lake model. Climatic. Change.,
795 129:471–483. Doi:10.1007/s10584-013-0978-y

796 Guo, YH., YS Zhang, N Ma, JQ Xu, and T Zhang (2019). Long-term changes in evaporation over
797 Siling Co Lake on the Tibetan Plateau and its impact on recent rapid lake expansion. Atmos.
798 Res., 216, 141-150. Doi: 10.1016/j.atmosres.2018.10.006

799 Haginoya, S., H Fujii, T Kuwagata, JQ Xu, Y Ishigooka, SC Kang and YJ Zhang (2009). Air-lake
800 interaction features found in heat and water exchanges over Nam Co on the Tibetan Plateau.
801 SOLA 5(1): 172-175. Doi: 10.2151/sola.2009-044

802 ——, H Fuiji, JH Sun and JY Liu (2012). Features of air-lake interaction in heat and water
803 exchanges over Erhai Lake. Journal of the Meterological Society of Japan, 90C: 55-73. Doi:
804 10.2151/jmsj.2012-C04

805 He, J., K Yang, WJ Tang, H Lu, J Qin, YY Chen and X Li (2020). Data Descriptor: The first
806 high-resolution meteorological forcing dataset for land process studies over China. Scientific
807 Data, 7(25): 1-11. Doi: 10.1038/s41597-020-0369-y

808 Hostetler, SW., GT Bates, and F Giorgi (1993). Interactive coupling of a lake thermal model with
809 a regional climate model. J. Geophys. Res., 98:5045–5057. Doi: 10.1029/92JD02843

810 Hook, SJ., FJ Prata, RE Alley, A Abtahi, RC Richards, SG Schladow and SO Palmarsson (2003).
811 Retrieval of lake bulk and skin temperature using Along-Track Scanning Radiometer
812 (ATSR-2) data: a case study using Lake Tahoe, California. Journal of Atmospheric and

Oceanic Technology 20(4):534-548. Doi: 10.1175/1520-0426(2003)20<534:ROLBAS>2.0.CO;2

Hu, HG and J Wang (2010). Modeling effects of tidal and wave mixing on circulation and thermohaline structures in the Bering Sea: Process studies. J. Geophys. Res., 115, C01006. Doi: 10.1029/2008JC005175

Huang, AN., YR Rao, and YY Lu (2010). Evaluation of a 3-D hydrodynamic model and atmospheric forecast forcing using observations in Lake Ontario. J. Geophys. Res., 115, C02004. Doi:10.1029/2009JC005601

——, Lazhu, JB Wang, YJ Dai, K Yang, N Wei, LJ Wen, Y Wu, XY Zhu, XD Zhang, SX Cai (2019). Evaluating and Improving the Performance of Three 1-D Lake Models in a Large Deep Lake of the Central Tibetan Plateau. J. Geophys. Res., Doi: 10.1029/2018JD029610

Huang, CJ and FL Qiao (2010). Wave-turbulance interaction and its induced mixing in the upper ocean. J. Geophys. Res., 115, C04026. Doi: 10.1029/2009JC005853

Huang, L., JB Wang, LP Zhu, JT Ju, and G Daut (2017). The Warming of Large Lakes on the Tibetan Plateau: Evidence From a Lake Model Simulation of Nam Co, China, During 1979–2012. J. Geophys. Res., 122, 13,095–13,107. Doi: 10.1002/2017JD027379

Kantha, LH. And CA Clayson (2004). On the effect of surface gravity waves on mixing in the oceanic mixing layer. Ocean Modelling, 6(2): 101-124. Doi: 10.1016/S1463-5003(02)00062-8

Ke, LH and CQ Song (2014). Remotely sensed surface temperature variation of an inland saline lake over the central Qinghai-Tibet Plateau. ISPRS Journal of Photogrammetry and Remote Sensing, 98: 157-167. Doi: 10.1016/j.isprsjprs.2014.09.007

Kirillin, G., LJ Wen and T Shatwell (2017). Seasonal thermal regime and climatic trends in lakes

836 of the Tibetan highlands. Hydrol. Earth Syst. Sci., 21, 1895-1909. Doi:
837 10.5194/hess-21-1895-2017

838 Lazhu, K Yang, JB Wang, YB Lei, YY Chen, LP Zhu, BH Ding, and J Qin (2016). Quantifying
839 evaporation and its decadal change for Lake Nam Co, central Tibetan Plateau. J. Geophys.
840 Res., 121, 7578-7591. Doi:10.1002/2015JD024523

841 Leon, LF., DCL Lam, WM Schertzer, DA Swayne and J Imberger (2007). Towards coupling a 3D
842 hydrodynamic lake model with the Canadian Regional Climate Model: Simulation on Great
843 Slave Lake. Environmental Modelling & Software 22, 787-796. Doi:
844 10.1016/j.envsoft.2006.03.005

845 Lei, YB., K Yang, B Wang, YW Sheng, B W.Bird, GQ Zhang and Ld Tian (2014). Response of
846 inland lake dynamics over the Tibetan Plateau to climate change. Climatic Change, 125:
847 281-290. Doi: 10.1007/s10584-014-1175-3

848 Li, ZG., SH Lv, YH Ao, LJ Wen, L Zhao, and SY Wang (2015) Long-term energy flux and
849 radiation balance observations over Lake Ngoring, Tibetan Plateau. Atmospheric Research
850 155:13-25. Doi: 10.1016/j.atmosres.2014.11.019

851 ——, YH Ao, SH Lv, JH Lang, LJ Wen, V Stepanenko, XH Meng, and L Zhao (2018).
852 Investigation of the ice surface albedo in the Tibetan Plateau lakes based on the field
853 observation and MODIS products. Journal of Glaciology, 1-11. Doi: 10.1017/jog.2018.35

854 Liu, HZ., JW Feng, JH Sun, L Wang and AL Xu (2015). Eddy covariance measurements of water
855 vapor and CO2 fluxes above the Erhai Lake. Science China: Earth Sciences, 58: 317-328.
856 Doi: 10.1007/s11430-014-4828-1

857 Long, Z., W Perrie, J Gyakum, R Laprise and D Caya (2007). Northern lake impacts on local
858 season climate. Journal of Hydrometeorology, 8(4): 881-896. Doi: 10.1175/JHM591.1

859 Lu, SL., J Ma, XQ Ma, HL Tang, HL Zhao and MHA Baig (2019). Time series of the inland
860 surface water dataset in China (ISWDC) for 2000-2016 derived from MODIS archives. Earth
861 Syst. Sci. Data, 11: 1099-1108. Doi: 10.5149/essd-11-1099-2019

862 Ma, RH., GS Yang, HT Duan, JH Jiang, SM Wang, XZ Feng, AN Li, FX Kong, B Xue, JL Wu and
863 SJ Lin (2011). China's lakes at present: Number, area and spatial distribution. Sci. China
864 Earth Sci, 54: 283-289. Doi: 10.1007/s11430-010-4052-6

865 Martynov, A., L Sushama and R Laprise (2010). Simulation of temperature freezing lakes by
866 one-dimensional lake models: performance assessment for interactive coupling with regional
867 climate models. Boreal Environment Research 15, 143-164.

868 Maussion, F., D Scherer, T Molg, E Collier, J Curio, and R Finkelnburg (2013). Precipitation
869 seasonality and variability over the Tibetan Plateau as Resolved by the High Asia Reanalysis.
870 J. Clim., 1910-1927. Doi: 10.1175/JCLI-D-13-00282.1

871 Mellor, GL and T Yamada (1982). Developmen of a turbulence closure model for geophysical
872 fluid problems. Reviews of Geophysics and Space Physics, 20(4): 851-875. Doi:
873 10.1029/RG020i004p00851

874 Mironov DV (2008). Parameterization of lakes in numerical weather prediction. Description of a
875 lake model [R]. COSMO technical report. Deutscher Wetterdienst, Offenbach am Main,
876 Germany.

877 Monismith, SG., J Imberger and ML Morison (1990). Convective motions in the sidearm of a
878 small reservoir. Limnol. Oceanogr., 35(8): 1676-1702.

879 Murakami, T., H Terai, Y Yoshiyama, T Tezuka, LP Zhu, T Matsunaka and M Nishimura (2007).
880 The second investigation of Lake Puma Yum Co located in the Southern Tibetan Plateau,
881 China. Limnology, 8:331-335. Doi:10.1007/s10201-007-0208-2

882 Notaro, M., A Zarrin, S Vavrus and V. Bennington (2013). Simulation of heavy lake-effect
883 snowstorms across the Great Lakes basin by RegCM4: Synoptic climatology and variability.
884 Mon. Wea. Rev., 141, 1990–2014. Doi:10.1175/MWR-D-11-00369.1

885 Nyamweya, C., C Desjardins, S Sigurdsson, T Tomasson, A Taabu-munyaho, L Sitoki and G
886 Stefansson (2016). Simulation of Lake Victoria circulation patterns using the Regional Ocean
887 Modelling System (ROMS). PLos ONE 11(3): e0151272. Doi:
888 10.1371/journal.pone.0151272

889 Qi, MM., XJ Yao, XF Li, HY Duan, YP Gao, and J Liu (2019). Spatiotemporal characteristics of
890 Qinghai Lake ice phenology between 2000 and 2016. J. Geogr. Sci. 2019, 29(1): 115-130.
891 Doi: 10.1007/s11442-019-1587-0

892 Rao, YR., MG Skafel and MN Charlton (2004). Circulation and turbulent exchange characteristics
893 during the thermal bar in Lake Ontario. Limnol. Oceanor., 49(6): 2190-2200. Doi:
894 10.4319/lo.2004.49.6.2190

895 Rao, YR and DJ Schwab (2007). Transport and mixing between the coastal and offshore waters in
896 the Great Lakes: a review. J. Great Lakes Res., 33:202-218.
897 Doi:10.3394/0380-1330(2007)33[202:TAMBTC]2.0.CO;2

898 Schwab, DJ and D Beletsky (2003). Relative effects of wind stress curl, topography, and
899 stratification on large-scale circulation in Lake Michigan. J. Geophys. Res. 108, 3044. Doi:
900 10.1029/2001JC001066

901 Sharma, A., AF Hamlet, HJS Fernando, CE Catlett, DE Horton, VR Kotamarthi, DAR Kristovich,
902 AI Packman, JL Tank, and DJ Wuebbles (2018). The Need for an Integrated

903 Land-Lake-Atmosphere Modeling System, Exemplified by North America's Great Lakes
904 Region. Earth's Future, 6, 1366–1379. Doi:10.1029/2018EF000870

905 Shepard D (1968). A two-dimensional interpolation function for irregularly-spaced data.
906 Proceedings of the 1968 ACM national conference, 27-29 August 1968, New York, pp
907 517-524. Doi: 10.1145/800186.810616

908 Song, CQ., B Huang, and LH Ke (2014). Inter-annual changes of alpine inland lake water storage
909 on the Tibetan Plateau, detection and analysis by integrating satellite altimetry and optical
910 imagery. Hydrological Processes 28(4), 2411-2418. Doi:10.1002/hyp.9798

911 Song, KS., M Wang, J Du, Y Yuan, JH Ma, GY Mu (2016). Spatiotemporal Variations of Lake
912 Surface Temperature across the Tibetan Plateau Using MODIS LST Product. Remote Sens., 8,
913 854. Doi:10.3390/rs8100854

914 Su, DS., XQ Hu, LJ Wen, SH Lyu, XQ Gao, L Zhao, ZG Li, J Du, and G Kirillin (2019). Numerical
915 study on the response of the largest lake in China to climate change. Hydrol. Earth. Syst. Sci.,
916 23, 2093-2109. Doi: 10.5194/hess-23-2093-2019

917 Subin, ZM., WJ Riley, and D Mironov (2012). An improved lake model for climate simulations:
918 Model structure, evaluation, and sensitivity analyses in CESM1. J. Adv. Model. Earth. Syst.,
919 4, M02001. Doi: 10.1029/2011MS000072

920 Titzel, DJ and JA Austin (2014). Winter thermal structure of Lake Superior. Limnol. Oceanogr.,
921 1336-1348. Doi: 10.4319/lo.2014.59.4.1336

922 Tolman HL (2009). User manual and system documentation of WAVEWATCH III version 3.14.
923 Tech. Note 276, NOAA/NWS/NCEP/EMC/MMAB, Camp Springs, Md

924 Tsydenov BO (2019). A numerical study of the thermal bar in shallow water during the autumn
925 cooling. Journal of Great Lakes Research, 45:715-725. Doi: 10.1016/j.jglr.2019.05.012

926 Verburg, P and JP Antenucci (2010). Persistent unstable atmospheric boundary layer enhances
927 sensible and latent heat loss in a tropical great lake: Lake Tanganyika. J. Geophys. Res., 115,
928 D11109. Doi: 10.1029/2009JD012839

929 Wan, W., PF Xiao, XZ Feng, H Li, RH Ma, HT Duan and LM Zhao (2014). Monitoring lake
930 changes of Qinghai-Tibetan Plateau over the past 30 years using satellite remote sensing data.
931 Chin. Sci. Bull., 59. Doi: 10.1007/s11434-014-0128-6

932 Wan, Z., Y Zhang, Q Zhang, and ZL Li (2004). Quality assessment and validation of the MODIS
933 global land surface temperature, Int. J. Remote Sens., 25, 261–274,
934 Doi:10.1080/0143116031000116417

935 Wang, BB., YM Ma, XL Chen, WQ Ma, ZB Su, and M Menenti (2015). Observation and
936 simulation of lake-air heat and water transfer processes in a high-altitude shallow lake on the
937 Tibetan Plateau. J. Geophys. Res. Atmos., 120,12,327–12,344. Doi: 10.1002/2015JD023863.

938 ——, YM Ma, WQ Ma, and ZB Su (2017a) Physical controls on half-hourly, daily, and monthly
939 turbulent flux and energy budget over a high-altitude small lake on the Tibetan Plateau. J.
940 Geophys. Res., 122:2289-2303. Doi:10.1002/ 2016JD026109

941 Wang, FS., GH Ni, WJ Riley, JY Tang, DJ Zhu and T Sun (2019). Evaluation of the WRF lake
942 module (v1.0) and its improvements at a deep reservoir. Geosci. Model Dev.,
943 12(5):2119-2138. Doi: 10.5194/gmd-2018-168

944 Wang, JB., LP Zhu, G Daut, JT Ju, X Lin, Y Wang, and XL Zhen (2009) Investigation of
945 bathymetry and water quality of Lake Nam Co, the largest lake on the central Tibetan Plateau.

946 Limnology, 10,149-158. Doi:10.1007/s10201-009-0266-8

947 ——, P Peng, QF Ma and LP Zhu (2010). Modern limnological features of Tangra Yumco and
948 Zhari Namco Tibetan Plateau. Journal of Lake Sciences, 22(4): 629-632

949 ——, L Huang, JT Ju, G Daut, Y Wang, QF Ma, LP Zhu, T Haberzettl, J Baade, and R
950 Mausbacher (2019). Spatial and temporal variations in water temperature in a high-altitude
951 deep dimictic mountain lake (Nam Co), central Tibetan Plateau. Journal of Great Lakes
952 Research. Doi: 10.1016/j.jglr.2018.12.005

953 ——, L Huang, JT Ju, ..., and BE Laval (2020). Seasonal stratification of a deep, high-altitude,
954 dimictic lake: Nam Co, Tibetan Plateau. Journal of Hydrology. Doi:
955 20.1016/j.jhdyrol.2020.124668

956 Wang, MD., JZ Hou and YB Lei (2014). Classification of Tibetan lakes based on variations in
957 seasonal lake water temperature. Chin. Sci. Bull., 59: 4847-4855. Doi:
958 10.1007/s11434-014-0588-8

959 Wang, XJ., GJ Pang and MX Yang (2017b). Review Precipitation over the Tibetan during recent
960 decades: a review based on observations and simulations. Int. J. Climatol. Doi:
961 10.1002/joc.5246

962 Wen, LJ., SH Lv, ZG Li, L Zhao, and N Nagabhatla (2015). Impact of two biggest lakes on local
963 temperature and precipitation in the Yellow River source region of the Tibetan Plateau.
964 Advances in Meteorology. Doi:10.1155/2015/248031

965 ——, SH Lv, G Kirillin, ZG Li, and L Zhao (2016). Air–lake boundary layer and performance of a
966 simple lake parameterization scheme over the Tibetan highlands. Tellus A: Dynamic
967 Meteorology and Oceanography, 68:1, 31091. Doi: 10.3402/tellusa.v68.31091

968 Wetzel, RG and GE Likens (2000). The heat budget of lakes. In: Limnological Analyses. Springer,
969 New York, NY. Doi: 10.1007/978-1-4757-3250-4_4

970 Wu, Y., AN Huang, B Yang, GT Dong, LJ Wen, Lazhu, ZQ Zhang, ZP Fu, XY Zhu, XD Zhang,
971 and SX Cai (2019). Numerical study on the climatic effect of the lake clusters over Tibetan
972 Plateau in summer. Clim. Dyn., Doi:10.1007/s00382-019-04856-4

973 Xiao, CL., BM Lofgren, J Wang, and PY Chu (2016). Improving the lake scheme within a coupled
974 WRF-lake model in the Laurentian Great Lakes. J. Adv. Model. Earth. Syst., 8, 1969–1985.
975 Doi:10.1002/2016MS000717

976 Xiao, F, L Ling, Y Du, Q Feng, Y Yan and H Chen (2013). Evaluation of spatial-temporal
977 dynamics in surface water temperature of Qinghai Lake from 2001 to 2010 by using MODIS
978 data. J. Arid Land, 5(4): 452-464. Doi: 10.1007/s40333-013-0188-5

979 Xu, LJ, HZ Liu, Q Du, and L Wang (2016). Evaluation of the WRF-lake model over a highland
980 freshwater in southwest China. J. Geophys. Res., 121. Doi: 10.1002/2016JD025396

981 ——, HZ Liu, Q Du, L Wang, L Yang, and JH Sun (2018). Differences of atmospheric boundary
982 layer characteristics between pre-monsoon and monsoon period over the Erhai Lake. Theor.
983 Appl. Climatol., 135: 305. Doi:10.1007/s00704-018-2386-8

984 Xu, YW., SC Kang, YL Zhang and YJ Zhang (2011). A method for estimating the contribution of
985 evaporative vapor from Nam Co to local atmospheric vapor based on stable isotopes of water
986 bodies. Chin. Sci. Bull., 56: 1511-1517. Doi: 10.1007/s11434-011-4467-2

987 Xue, PF, DJ Schwad and S Hu (2015). An investigation of the thermal response to meteorological
988 forcing in a hydrodynamic model of Lake Superior. J. Geophys. Res. Oceans, 120:
989 5233-5253. Doi: 10.1002/2015JC010740

990 ——, JS Pal, XY Ye, JD Lenters, CF Huang, and PY Chu (2016). Improving the Simulation of

Large Lakes in Regional Climate Modeling: Two-Way Lake–Atmosphere Coupling with a 3D Hydrodynamic Model of the Great Lakes. J. Clim., 1605-1627. Doi:10.1175/JCLI-D-16-0225.1

Yan, FQ., M Sillanpaa, SC Kang, KS Aho, B Qu, D Wei, XF Li, CL Li, and P A.Raymond (2018). Lakes on the Tibetan Plateau as conduits of greenhouse gases to the atmosphere. J. Geophys. Res., 123. Doi: 10.1029/2017/JG004379

Yang, XY., YQ Lv, YM Ma and J Wen (2015) Summertime thermally-induced circulations over the Lake Nam Co region of the Tibetan Plateau. J. Meteorol. Res., 29, 305-314. Doi: 10.1007/s13351-015-0424-z

Zhang, GQ., TD Yao, SL Piao, T Bolch, HJ Xie, DL Chen, YH Gao, CM O'Reilly, CK Shum, K Yang, Y Shuang, YB Lei, WC Wang, Y He, K Shang, XK Yang, and HB Zhang (2017). Extensive and drastically different alpine lake changes on Asia's high plateaus during the past four decades. Geophys. Res. Lett., 44, 252–260. Doi:10.1002/2016GL072033

—— (2018). Changes in lakes on the Tibetan Plateau observed from satellite data and their responses to climate variations [J]. Progress in Geography, 37(2): 214-223. Doi: 10.18306/dlkxyj.2018.02.004

Zhang, X., KQ Duan, PH Shi, and JH Yang (2016). Effect of lake surface temperature on the summer precipitation over the Tibetan Plateau. J. Mt. Sci., 13(5):802-810. Doi:10.1007/s11629-015-3743-z

Zhang, QH., JM Jin, LJ Zhu and SL Lu (2018). Modelling of water surface temperature of three lakes on the Tibetan Plateau using a physically based lake model. Atmosphere Ocean, 2018, 1-7. Doi: 10.1080/07055900.2018.1474084

Zhu, LJ, JM Jin, X Liu, L Tian, and QH Zhang (2017). Simulations of the impact of lakes on local

and regional climate over the Tibetan Plateau. Atmosphere Ocean 1-10. Doi:10.1080/07055900.2017.1401—524

Table 1. The bimonthly lake-averaged lake surface temperature (LST, unit: °C) from MODIS observation and POM/WRF-Lake simulation. The root mean square error (RMSE, unit: °C) between the simulation and observation is also presented.

	May-Jun		**Jul-Aug**		**Sep-Oct**		**Nov-Dec**	
	LST	RMSE	LST	RMSE	LST	RMSE	LST	RMSE
MODIS	5.74	—	10.74	—	9.38	—	3.69	—
POM	6.02	1.85	11.57	1.15	9.85	0.66	4.12	0.96
WRF-Lake	6.04	1.78	11.01	0.93	8.20	1.30	1.09	3.05

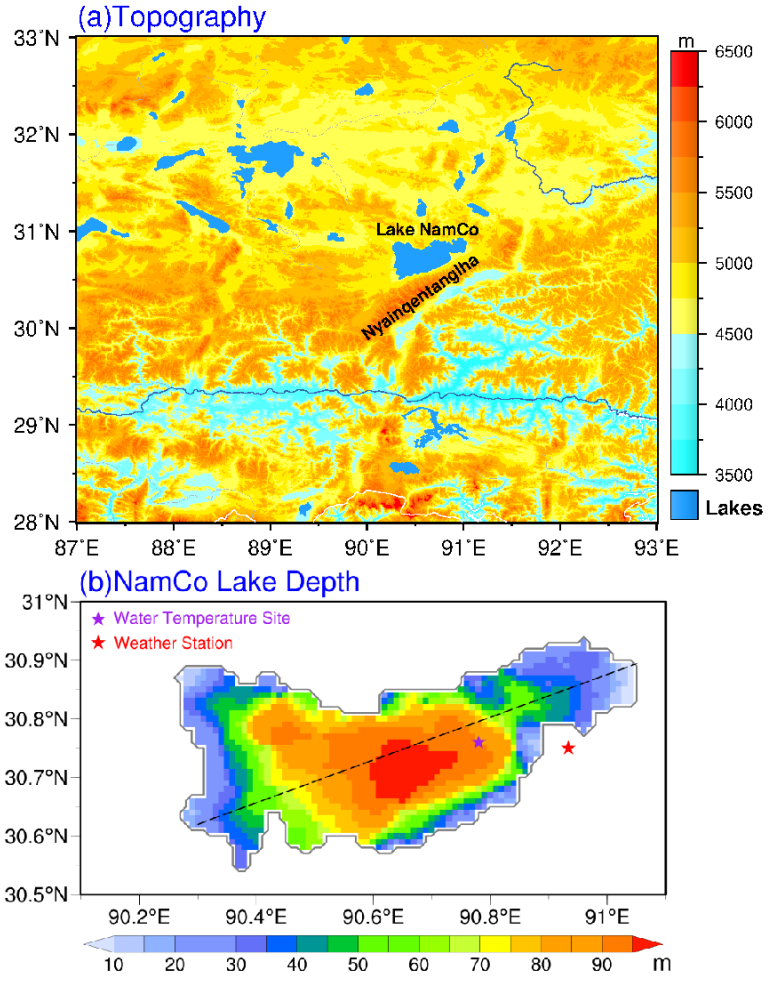

1026

1027 **Figure 1.** (a) Spatial distribution of the topography (unit: m) and lakes over central TP; (b) the

1028 1-km POM/WRF-Lake grid bathymetry of LNC (unit: m). The purple and red asters represent

1029 the water temperature site and the weather station, respectively. The dashed line denotes the

1030 southwest-northeast transection used in Figures 8 and 9.

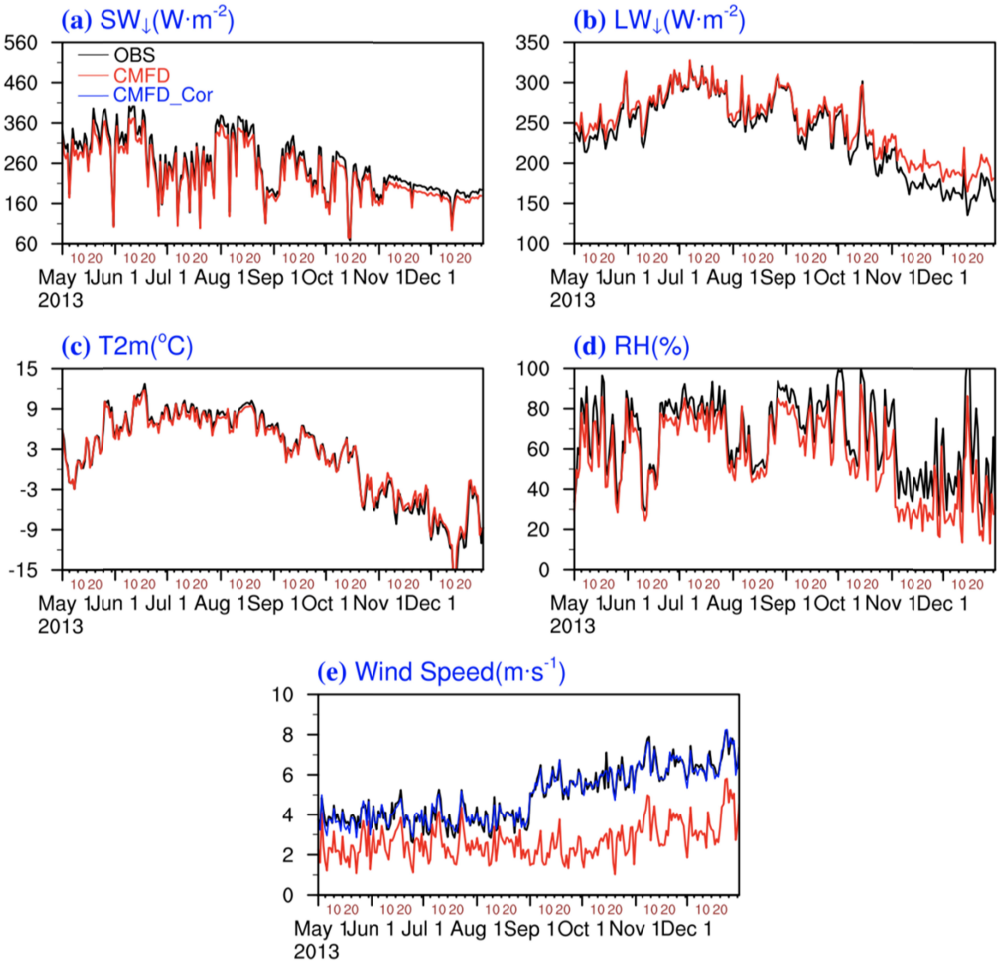

Figure 2. The daily in-situ (black lines) and CMFD (red curves) surface downward shortwave radiation(a), downward longwave radiation (b),2-m air temperature (c), 10m relative humidity (d), and 10m wind speed (e) during 1th May to 31st December 2013. The blue line in (e) denotes the calibrated wind speed by piecewise linear regression.

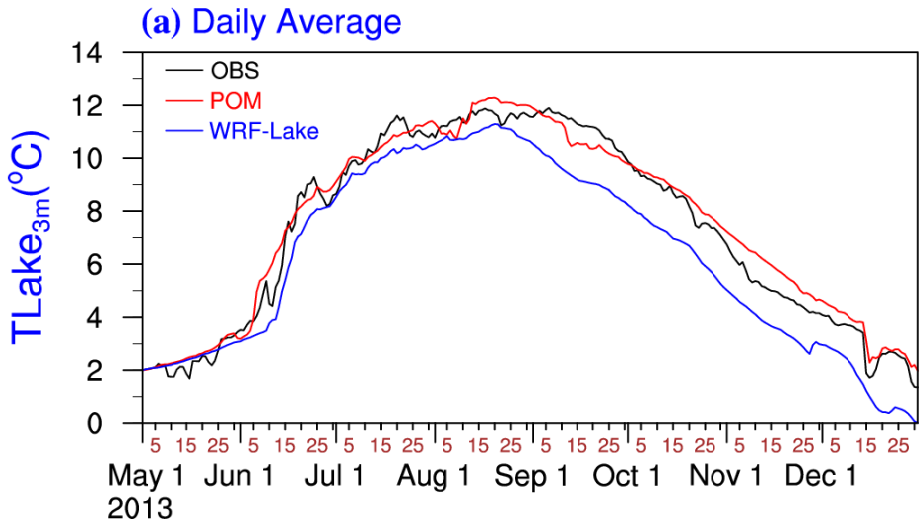

1037

1039 **Figure 3.** The daily $TLake_{3m}$ from the station measurements, the POM and WRF-Lake

1040 simulations at the observation site during 1th May to 31st December 2013.

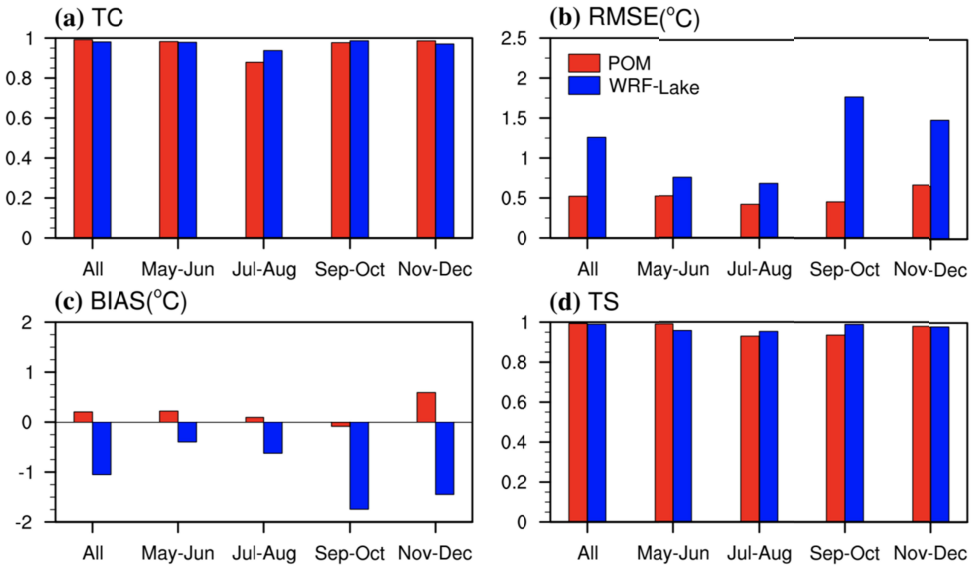

1040

1042 **Figure 4.** (a) TC, (b) RMSE, (c) BIAS, and (d) TS between the POM/WRF-Lake modelled

1043 and observed daily $TLake_{3m}$ during the whole and bimonthly simulation periods.

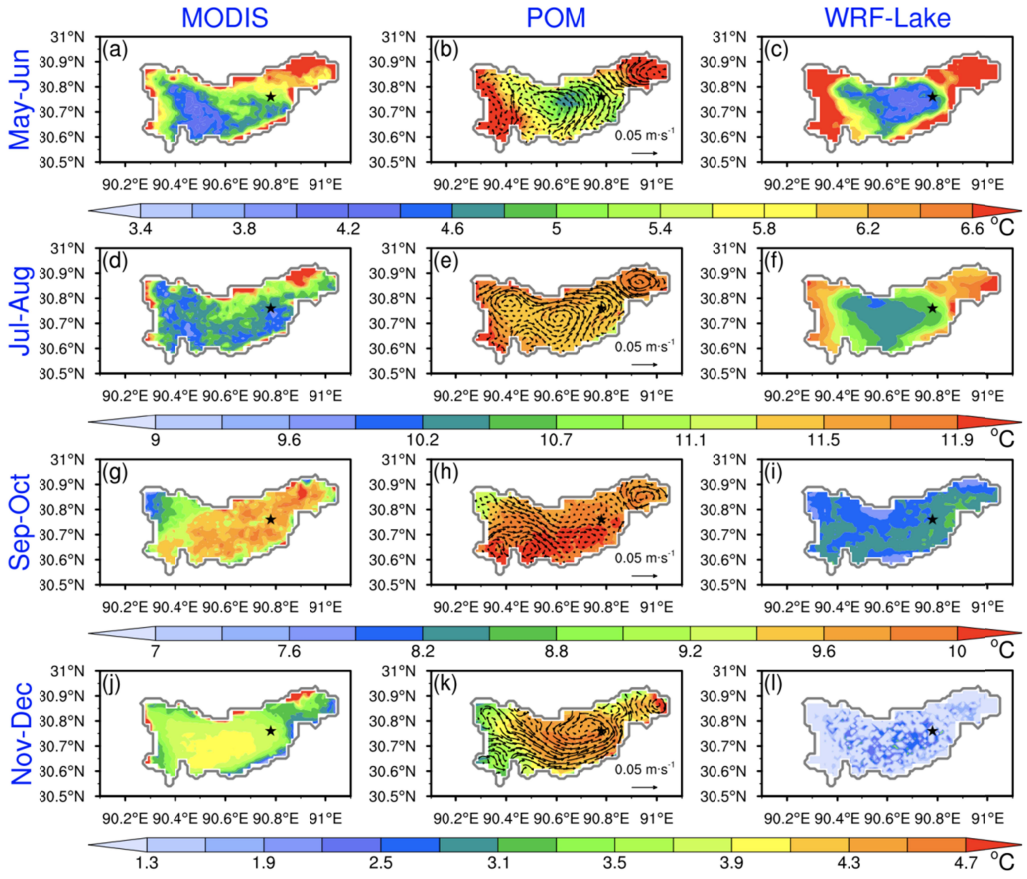

1043

1047 **Figure 5.** (a) MODIS retrieved, (b) POM, and (c) WRF-Lake simulated bimonthly averaged LST

1048 over the LNC during May-December 2013. The vectors in the middle panel represent the water

1049 currents averaged over the surface layers (0-3m). The black asters denote the water temperature

1050 site.

1048

1049

1050

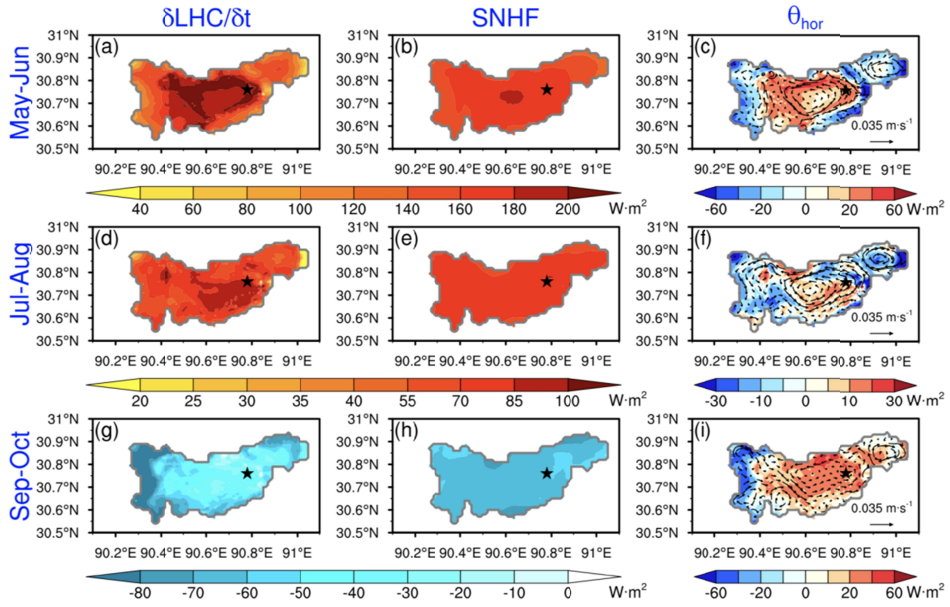

1051

1054 **Figure 6.** The bimonthly averaged heat budget components: rate of change in lake heat content

1055 $\delta LHC/\delta t$, surface heat flux SNSL, and horizontal heat exchange θ_{hor} (all units: W·m^{-2}) over

1056 LNC during 2013. All the above variables are calculated based on POM results.

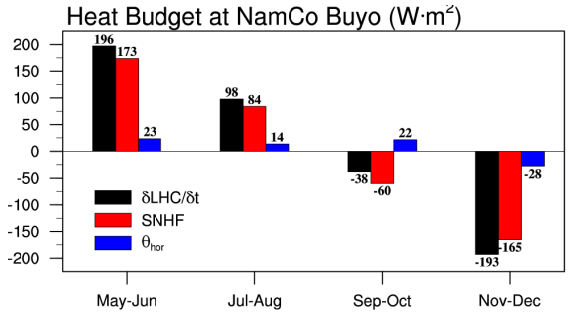

1055

1056 **Figure 7.** Same as Figure 6, but for the heat budget at the water temperature site over LNC.

1057

1058

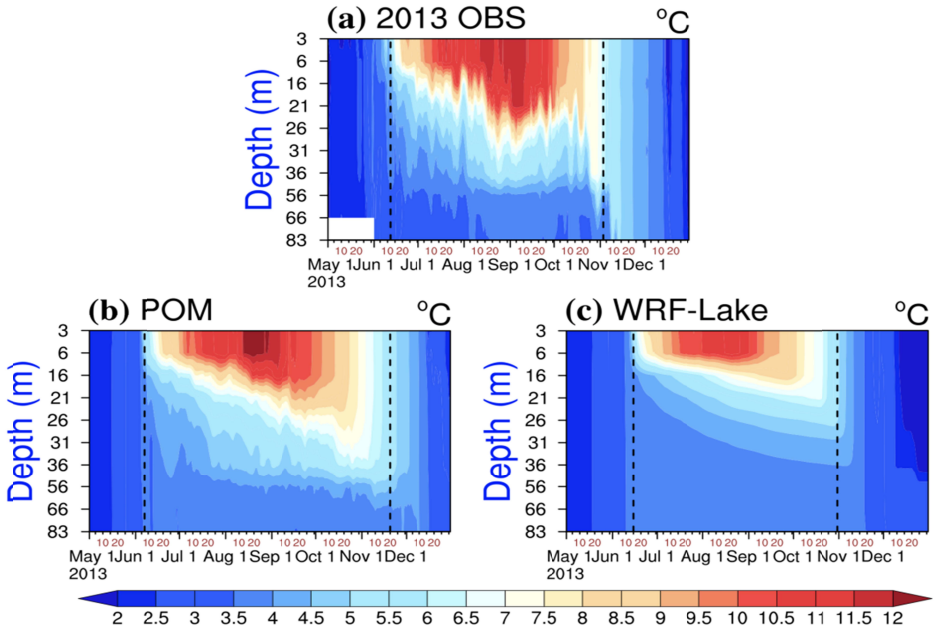

1059

1062 **Figure 8.** Time-depth distributions of the daily mean lake temperature from (a) the observation,

1063 (b) POM, and (c) WRF-Lake simulations at the water temperature site during 1thMay to 31st

1064 December 2013. The black dashed lines indicate the onset and end of lake thermal stratification.

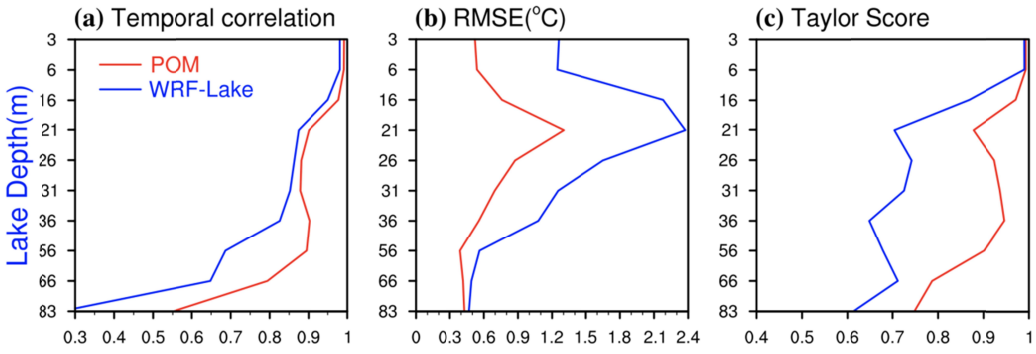

1063

1065 **Figure 9.** The vertical distributions of the (a) TC, (b) RMSE, and (c) TS for the daily mean lake

1066 water temperature simulated by POM/WRF-Lake against the 10-layer in-situ observations.

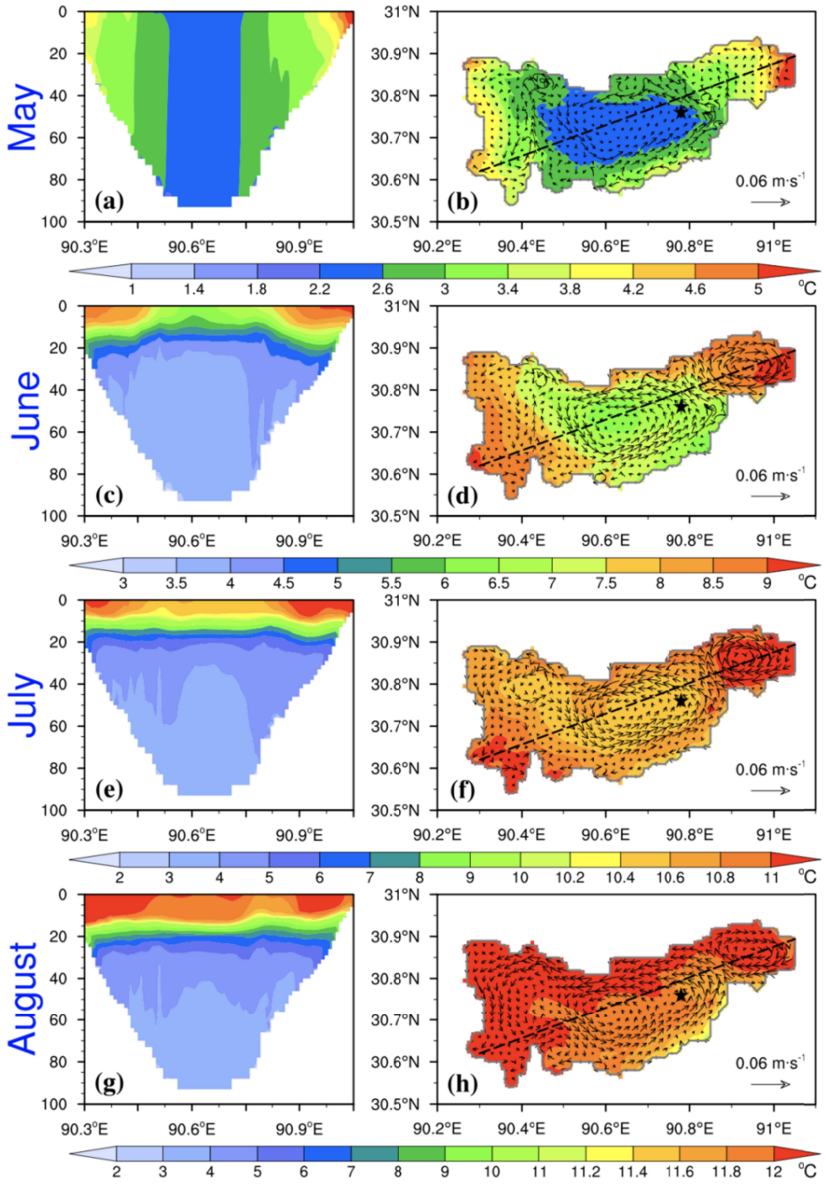

Figure 10. Monthly averaged (a, c, e, g) lake temperature along the southwest-northeast transection, (b, d, f, h) LST and depth-averaged currents over LNC during May-August 2013. In (b, d, f, h), the black dashed lines denote the transection and the black solid asters represent the location of Nam Co water temperature site.

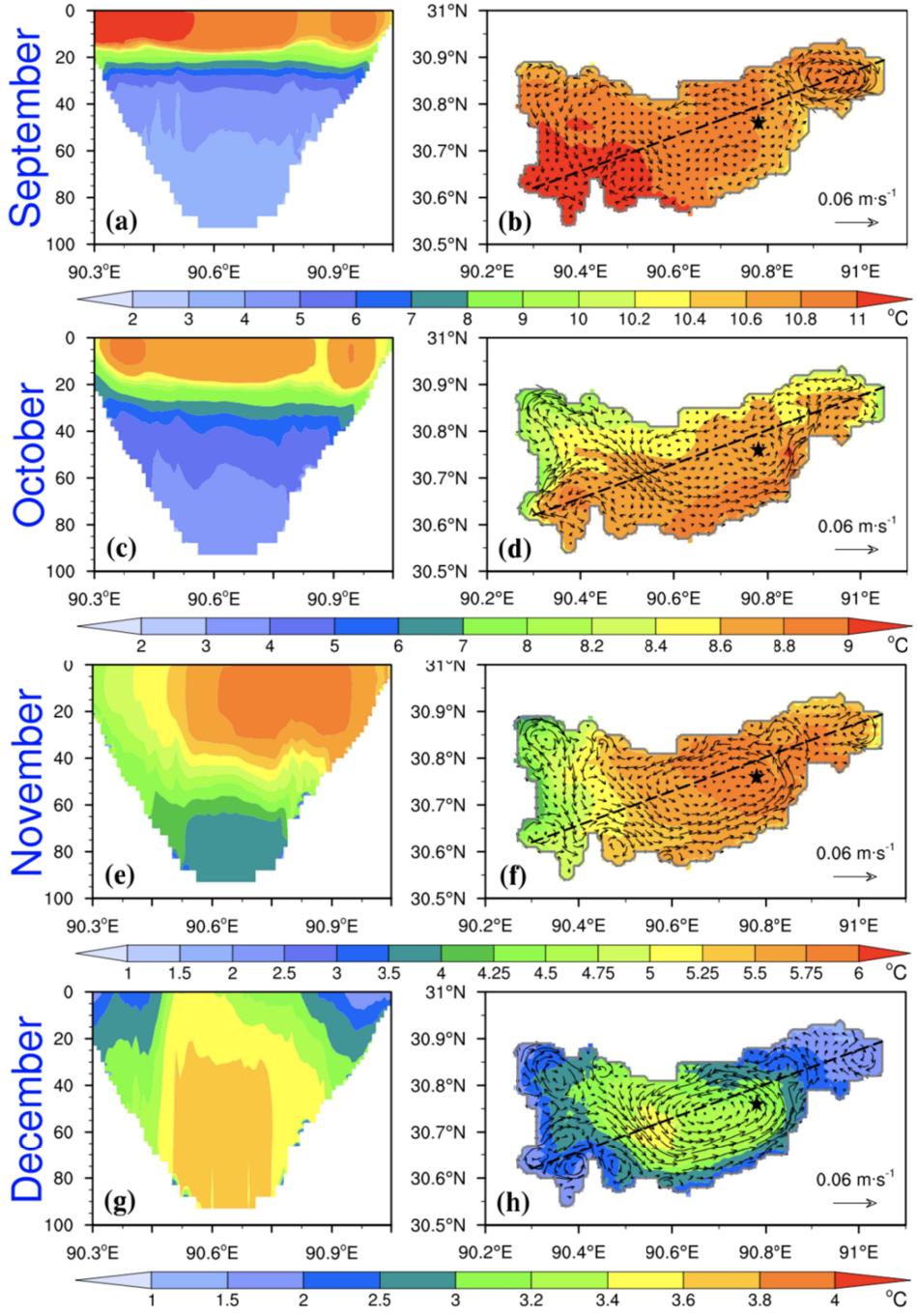

Figure 11. same as Figure 8, but for the period during September-December 2013.